Synchrotron Studies of Electronic and Magnetic Properties of Oxide Heterostructure Interfaces

A thesis submitted to the
College of Graduate and Postdoctoral Studies
in partial pulfillment of the requirements
for the degree of Master of Science
in the Department of Physics and Engineering Physics
University of Saskatchewan
Saskatoon

By
Niyusha Hosseini

Permission to Use

In presenting this thesis in partial fulfillment of the requirements for a Postgraduate degree from the University of Saskatchewan, I agree that the Libraries of this University may make it freely available for inspection. I further agree that permission for copying of this thesis in any manner, in whole or in part, for scholarly purposes may be granted by the professor or professors who supervised my thesis work or, in their absence, by the Head of the Department or the Dean of the College in which my thesis work was done. It is understood that any copying or publication or use of this thesis or parts thereof for financial gain shall not be allowed without my written permission. It is also understood that due recognition shall be given to me and to the University of Saskatchewan in any scholarly use which may be made of any material in my thesis.

Disclaimer

Reference in this thesis to any specific commercial products, process, or service by trade name, trademark, manufacturer, or otherwise, does not constitute or imply its endorsement, recommendation, or favoring by the University of Saskatchewan. The views and opinions of the author expressed herein do not state or reflect those of the University of Saskatchewan, and shall not be used for advertising or product endorsement purposes. Unless otherwise noted, copyright of the material in this thesis belongs to the author.

Requests for permission to copy or to make other uses of materials in this thesis in whole or part should be addressed to:

Head of the Department of Computer Science
176 Thorvaldson Building, 110 Science Place
University of Saskatchewan
Saskatoon, Saskatchewan S7N 5C9 Canada

OR

Dean
College of Graduate and Postdoctoral Studies
University of Saskatchewan
116 Thorvaldson Building, 110 Science Place
Saskatoon, Saskatchewan S7N 5C9 Canada

Abstract

This thesis focuses on two projects involving resonant x-ray experiments on transition metal oxide heterostructures. The first project is the study of the interface between the anti-ferromagnetic Mott-Hubbard insulator $LaTiO_3$ and the anti-ferromagnetic charge transfer insulator $LaFeO_3$, which has previously been observed to exhibit interfacial charge transfer. The goal is an understanding of complex charge transfer and magnetic properties of the interface, which may provide insight into useful functionalities of the interface and possible use in electronic and magnetic devices. First, background information on the $3d$ elements and components forming this interface is given, the experimental techniques used to study the interface and methods to analyse the acquired data by Prof. Green are described. A combination of resonant x-ray reflectometry and x-ray absorption spectroscopy allowed us to verify the structural quality of the interface, detect the interface charge transfer, and determine the spin state of relevant atoms. For the second project of this thesis, we study the role of oxygen vacancies in forming 2D electron liquid (2DEL) at the interface of $LaAlO_3/SrTiO_3$, a conducting sheet of charge which emerges between two otherwise insulating materials. Previous studies of this interface have revealed that it exhibits electrical conductivity, superconductivity and ferromagnetism. The fields of oxide interfaces in general, and oxide 2D electron liquids in particular, are currently of high interest as they show great potential for device applications. Our experiments study the luminescence of these interface oxygen vacancies, using X-ray-excited optical luminescence (XEOL), in a set of samples where variation in growth conditions were used as an attempt to control the distribution profile of oxygen vacancies. By modifying the incident photon energy during XEOL experiments, we control the probing depth of our x-rays which stimulate the luminescence of the oxygen vacancies, and thus probe their depth profile. Our resulting depth profiles can distinguish if the oxygen vacancies are fully confined to the interface where the 2DEL resides, or if they are distributed further into the substrate. These results give key insight into the interaction between vacancies and conduction electrons, and how to achieve high mobility electron liquids.

Acknowledgements

I would like to express my utmost appreciation to my supervisor, Dr. Robert J. Green for his extremely caring supervision and guidance. From our very first meeting, his enthusiasm for what he works on made me sure I would be in the best environment. Whether in our every regular meetings or in the experimental parts of our research in CLS, he created an amazing atmosphere in which he was patiently focused on my learning. His guidance through every step of my master program was the perfect lever to lift me through every hardship and motivated me to partake in tasks that were challenging for me. With his supportive supervision I was able to explore many aspects of research and begin to find my true passion in the best way that I could have imagined. He was there for every difficult moment of my graduate life and as I continue learning, I hope to have his brilliant scientific point of view and keen mind.

I would also like to thank my committee members and the main office staff of the Department of Physics and Engineering Physics for all their efforts. I appreciate members of U of S Condensed Matter Physics Group for the many helpful and insightful discussions and interactions that I have had with them: Patrick and Tristan.

It is a pleasure to thank my great friends who have always been a major source of support, encouragement and fruitful discussions during all single moments of my master program: Bardia: the true friend whose company was the warmth in the midst of every cold moment in Saskatoon, Florence: who encouraged me to continue down my path and supported me through every step. Igor: who was always there for interesting discussions and support.

I thank my mother Narges for her unconditional and selfless support and my brother Aria for his friendship, encouragement and wonderful support from very far. My most heartfelt appreciation belongs to Ayub, words cannot describe his love and support through my life from previous chapters till the very end of my graduate program. He closely shared every hardship and wonderful moments of my life with me.

To Ayub

Contents

List of Tables

List of Figures

1 Introduction

Condensed matter physics exploits both experimental and theoretical physics in the manner of measuring different materials and studying their properties using various experimental methods along with developing mathematical models to understand their physical behavior. The evolving of modern material science started as early as the mining era and led to metallurgy which played a significant role in the breakthroughs in the late 19^{th} century [1]. With the beginning of the space race, understanding and engineering of metallic alloys and materials needed to build space vehicles became of utmost interest [2]. Since then, this field has been evolving along side the need of development in revolutionary technologies. Additionally, many of the current scientific problems are strongly correlated with materials, as the basis of devices and modern society relies on the available materials and how they are used. Thus a breakthrough in materials science will most likely affect technology in many aspects.

The base of material science is relating the properties of different materials to their structure in order to study the relative performance of materials in a given application. The main factors in determining the structure-properties correlation are the chemical elements and the way they were processed into their final form. Then relating the characteristic properties to laws of thermodynamics and kinetics, gives the general understanding of the materials detailed structure.

Many of the recent developments in condensed matter physics focus on complex oxide heterostructures and their interfaces, due to their interesting electric and magnetic properties, the possibility of being tuned to the desired stage and promising applications in many fields such as electronics. One of the most recent focused examples is the 2D electron layer formed between layers in certain heterostructures which is an excellent candidate for examining the tunablity of materials.

A notable example of such a 2D electron layer is the formation of a two-dimensional electron gas at the (001) interface between the two band insulators $SrTiO_3$ (STO) and $LaAlO_3$ (LAO) [3]. There are various ideas developed to explain this system, many of them related to the fact that

ionic and hetero-polar films of certain orientations consist of charged planes: This would lead to a sizeable potential along the film normal (polar catastrophe), unless its polar interfaces carry opposite compensating charges [4].

In this thesis one of our primary objectives is to extract a depth profile of donor oxygen vacancies near buried interfaces in thin film heterostructures which contain 2D electron liquids (2DELs). We used X-ray Eminent Optical Luminescence (XEOL) spectroscopy to determine if the oxygen vacancies are fully confined to the interface where the 2DEL resides, or if they are distributed further into the substrate. This will give key insight into the interaction between vacancies and conduction electrons, and how to achieve high mobility electron liquids.

Very little is known about the confinement of the oxygen vacancies to the interface in such systems, how film growth conditions affect their concentration and distribution, or their detailed depth distribution into the substrate [5]. If we can address these issues using our XEOL-based extraction of the oxygen vacancy distribution, it will be a great leap forward for this very active research field.

Another objective of this thesis is the study of an interface between the anti-ferromagnetic Mott-Hubbard insulator $LaTiO_3$ and the anti-ferromagnetic charge transfer insulator $LaFeO_3$ based on existing data. Previous works [6] have indicated that this interface may exhibit atomic-scale transfer and a special non-magnetic Fe^{2+} layer, which are both difficult to detect and characterise. Using Resonant X-ray Reflectometry (RXR) on several samples, the main goal is to quantify charge transfer at the interface and determine subsequent changes in magnetic properties driven by this charge transfer. It is noteworthy to say that controlling the number of transferred electrons and hence the properties of the interface, opens up new pathways to design optimal functioning oxide interfaces [7].

1.1 Transition Metals and Transition Metal Oxides

Transition metals and their compounds are of particular interest due to their unique properties, which can be enhanced and tuned at complex interfaces. This chapter will provide some necessary background information on their properties and relevant emergent phenomena. The materials studied to accomplish the goals of this thesis rely on very specific behaviours of transition metals and

their compounds. First, we will define which elements we precisely mean when we discuss transition metals. Next we will describe the physics behind some important properties of both isolated transition metal atoms, and transition metal atoms in solids.

A transition metal is described as any element in the d-block of the periodic table, which includes groups 3 to 12 on the periodic table, as shown in Figure 1.1. Special properties of this block of the table include for example magnetism and superconductivity, and elements within this block are responsible for the colours of many materials. More specifically, our studies involve materials containing selected elements from the top row of this block [7, 8].

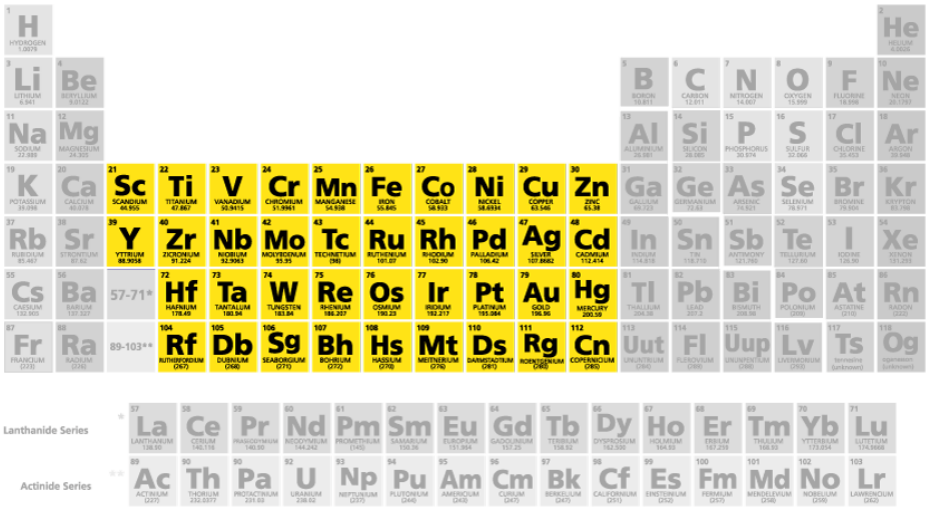

Figure 1.1: Transition metals in periodic table. Image reproduced from [9].

An important feature of the 3d elements is the lack of nodes in their radial wave functions- a schematic for hydrogen-like orbitals shown in Figure 1.2, which results in localisation of the 3d electrons and thus relatively weak participation in chemical bonding. Recalling the quantum mechanics, different electron shells and orbitals like the 3d orbitals, the typical solution of the Schrödinger equation for a hydrogen-like atom (the only case where analytic solutions are available) leads to electron wavefunctions which are separated into an angular part and a radial part. The behaviours of these wavefunctions are governed by the quantum numbers which arise as part of the solution. In particular, the shapes of the radial wavefunctions are governed by both the principal (n) and azimuthal (l) quantum numbers. For the case of 3d wavefunctions (as well as 1s, 2p, and

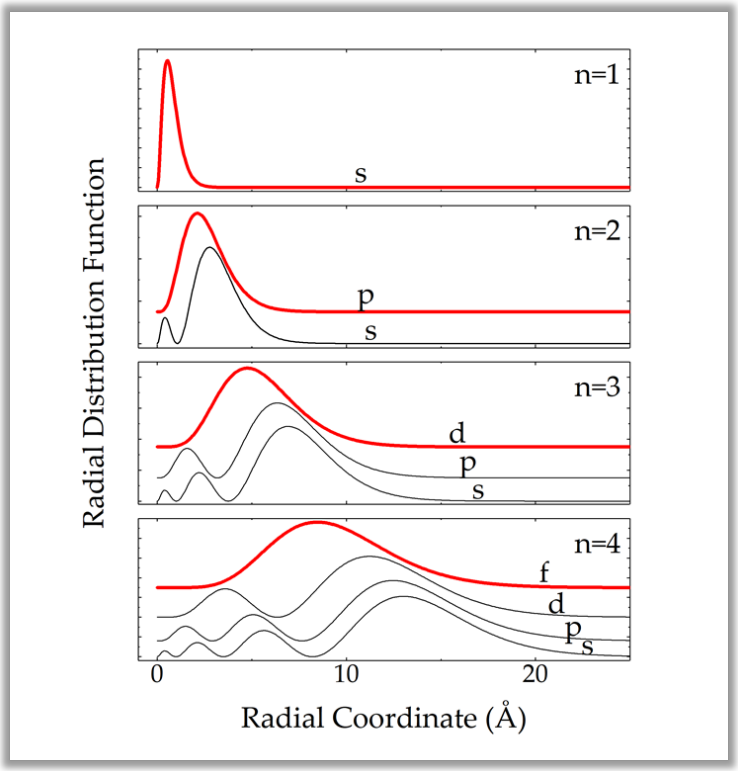

Figure 1.2: A schematic of the radial distribution wavefunction for hydrogen-like orbitals. Image reproduced from [8].

4f), there are no radial nodes, and this leads to the wavefunctions being more contracted toward the nuclear charge and therefore more localized. In this case, because they are more localized, the different 3d electrons strongly interact with each other, leading to what is called "electron correlation" [8].

In these materials 4s electrons are usually lost first upon oxidation since the 4s shell is less bound to the nucleus than the 3d or the filling valance shell. Some interesting properties common in Transition Metal Oxides (TMOs) are:

Charge transfer transitions: When an electron jumps from an initial orbital to an empty or partially filled orbital, there is a charge-transfer transition. In transition metal oxides, the most common type of charge transfer occurs from an oxygen 2p orbital into the partially filled transition metal 3d shell. Based on the donor and accepter, we can have different types of charge transfer. Such transitions are more prominent when the metal is in a high oxidation state.

Magnetism: Transition metal compounds can be paramagnetic (when they have one or more unpaired valence electrons, but no long range order), diamagnetic (when shells are completely full, or the energetic splittings are such that all electrons pair up), ferromagnetic (long range spontaneous magnetic order, even in absence of applied field), and anti-ferromagnetic (caused by alignment of individual spins in a regular but cancelling pattern according to neighbouring sublattices). For transition metal oxides, strong correlation in the motion of each electron leads to the fact that the spin of an ion can be better defined by one total spin than each individual electron spins. Thus transition metal oxides can have different internal magnetic fields or different response to applied magnetic field; relative to their number, magnitude and orientation of the spin sublattices [10].

Superconductivity: A certain material is called superconductor when it has no electrical resistance and no magnetic flux fields. In ordinary metallic conductors, as the temperature lowers down to near absolute zero, the resistance decreases gradually. However, in a superconductor below its critical temperature the resistance drastically drops to zero. Characteristics of superconductivity in materials appear when the temperature T is lowered below a critical temperature T_c that varies in different superconductors. In $LaAlO_3/SrTiO_3$ interfaces, superconductivity was first observed in 2007, with a critical temperature of $\sim$200 mK. Like its conductivity, the superconductivity in this material seems to be two-dimensional [11, 12].

Transition metals can form compounds in many oxidation states, because of the relatively low energy gap between possible oxidation states that they can take. Transition metal oxides are the result of oxygen atoms bonding with transition metals. Transition metal oxides have useful catalytic properties, and are also frequently used for producing pigments in paints and plastics, mostly titanium dioxide. They have a wide variety of surface structures, which affect their chemical properties [13]. As many of these oxides only slightly differ from each other and their structures are similar so they can be constricted from the same building blocks, one oxide can convert to another by the process of oxidation or reduction [10].

Many transition metal oxides have the perovskite structure with chemical formula ABO_3, which consists of one large (A) and one small cation (B) [14]. See Figure 1.3 for a visualization of the perovskite structure. In this structure, there is a simple cubic array of B cations, with the A cations occupying the centre of the cube, and the oxygen atoms are located at the centre of the 12 edges

of the simple cube [14]. Defect sites can interfere with the stability of metal oxide surfaces, so it is important to locate and determine methods to control these sites [14].

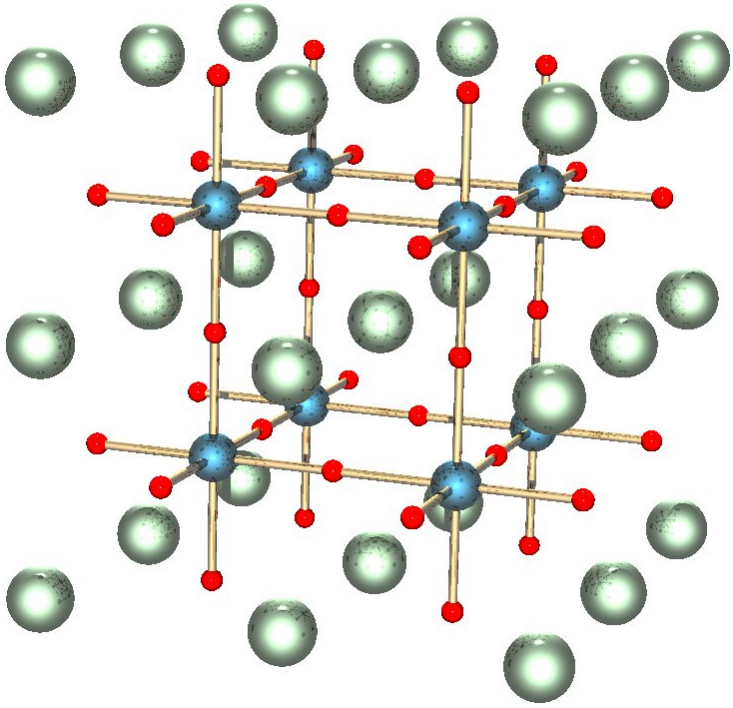

Figure 1.3: Structure of a perovskite with general chemical formula ABO_3. The red spheres in our case are oxygen atoms, the blue spheres are B atoms (a smaller metal cation, such as Ti^{4+}), and the green spheres are the A atoms (a larger metal cation, such as Sr^{2+}). Pictured is the undistorted cubic structure; the symmetry is lowered to orthorhombic, tetragonal or trigonal in many perovskites. Figure reproduced from [14].

One of the transition metal elements in this research is titanium which is a chemical element with the symbol Ti and atomic number 22. It is a shiny, silver-coloured metal with low density and high strength. Titanium can be alloyed with iron, aluminium, vanadium, and molybdenum, among other elements, to produce strong, lightweight alloys for aerospace, automotive, agriculture, mobile phones, and many other applications. The two most useful properties of titanium are corrosion resistance and strength-to-density ratio, the highest of any metallic element. In its unalloyed condition, titanium is as strong as some steels, but less dense [15]. The 22 electrons of titanium are arranged in the configuration $[Ar]3d^2 4s^2$, of which the 3d and 4s electrons are relatively close in energy, and thus it can lose a variable number of electrons [15].

1.2 Heterostructures and Thin films

Heterostructures made of TMOs are known to exhibit a wide variety of properties such as superconductivity at interfaces of non-superconducting copper oxides, possibility of finding superconductivity and ferromagnetism simultaneously and orbital reconstruction [4]. These interesting properties are mainly possible due to the structural, electric and magnetic degrees of freedom.

A heterojunction is the interface between layers or regions of two different solid-state materials, including crystalline and amorphous structures of metallic, insulating, fast ion conductor and semiconducting materials [16]. With these materials having unequal band gaps, engineering the electronic band gaps is beneficial in many device applications such as transistors. Heterostructures are made of combining multiple heterojunctions.

At the heterointerface between two semiconductors the difference in work functions is resolved via charge transfer. Understanding the mechanism of charge transfer will better help in determining the origin of charge carriers and designing growth sequences [17]. The importance of configuration of band alignment, while being quite well known in conventional semiconductors, has led to many different experimental studies on oxides during recent years [17]. Considering the fact that the energy bands in correlated oxides vary dramatically with change in several factors such as doping and strain, the charge transfer at complex oxide interfaces is generally much more complex [17].

In order to obtain fine quality thin films for device applications and for better understanding of properties, the concepts regarding the nature of the films should be understood. The ideal condition of the film formation involves the deposition of the material atom by atom (or molecule by molecule) and layer by layer with proper time interval between the two successive depositions so that, they can occupy the minimum potential energy configuration with respect to the substrate and subsequently on the previously deposited layers [10]. In a thermodynamically stable film all atoms should be in their minimum potential energy sites and the incoming atoms will take up positions and orientations energetically compatible with the neighbouring atoms of the substrate or to the previously deposited layers [10].

By combining heterostructures we can obtain a thin film which is a very thin solid layer of material (with thickness in the sub-nanometer to micron region) deposited on a substrate and is therefore bounded by a solid-solid interface and by its surface (film-vacuum interface) [18]. It can

mathematically be defined as a solid material confined between two parallel planes and extended infinitely in two directions (x, y) but restricted along the third direction (z), which is perpendicular to the x-y plane. The dimension along z-direction is known as the film thickness (d or t). The properties of a thin film depend significantly on the properties of its interfaces. There are many interesting interfaces currently under research, which have incredible properties and functions in many fields such as semiconductor device fabrication; in some cases the interface will demonstrate metallic conductivity, even though the super lattice structure is based on two insulators [19]. In addition, there have been reports of superconductive behaviour [20].

Thin-film deposition processes and corresponding applications is a growing complex field with many developments, one of which may be the so-called epitaxial growth of materials. Here, epitaxy is defined as the oriented overgrowth of the film material, which typically results in single crystal films [21]. In the deposition of crystalline thin films, the films often grow following the crystalline structure of the substrate. This technology is used, for instance, to grow a film, which is more pure than the substrate, has a lower density of defects, and to fabricate layers having different doping levels.

In order to study the properties of a grown crystal it is useful to understand the process of the films interacting with light and specifically x-rays. As light shines on the surface of a film, it is partially transmitted and partially reflected at the top surface. The transmitted part reaches the bottom surface and may once again be transmitted and reflected. The Fresnel equations provide a quantitative description of how much of the light will be transmitted and how much will be reflected at each interface. Fresnel's equations provide the transmission and reflection coefficients for waves. The reflectance for s-polarised, also known as transverse-electric (TE) or σ-polarised light travelling from medium 1 to medium 2 is:

$$R_s = |\frac{n_1 \cos\theta_i - n_2 \cos\theta_t}{n_1 \cos\theta_i + n_2 \cos\theta_t}|^2, \tag{1.1}$$

While the reflectance for p-polarised, also known as Transverse-Magnetic (TM), π-polarised, or tangential plane polarised light is:

$$R_p = |\frac{n_1 \cos\theta_t - n_2 \cos\theta_i}{n_1 \cos\theta_t + n_2 \cos\theta_i}|^2; \tag{1.2}$$

in which incident and transmitted angles with respect to the normal of the incidence are denoted as θ_i and θ_t, respectively. The refractive index of medium 1 is n_1 and medium 2 has the refractive index of n_2.

The relation of the transmitted light to the reflected light power, excluding the fraction of light that might be absorbed, can be deducted from conservation of energy:

$$T_{s(p)} = 1 - R_{s(p)}. \tag{1.3}$$

The relation between θ_i and θ_t can be implemented in the equation, using Snell's law:

$$n_1 \sin\theta_i = n_2 \sin\theta_t. \tag{1.4}$$

The light reflected from the upper and lower surfaces will interfere. The degree of constructive or destructive interference between the two light waves depends on their phase difference. This difference is a function of the thickness of the film layer, the refractive index of the film, and the angle of incidence of the original wave on the film. Some of the most important functions of transition metals, are functional units in multilayer devices and buffer layers to relieve strain and control termination. The distribution of atoms of different elements in and around buried layers often greatly affects their electronic phase behaviour and functionality, which has led to an escalating demand for chemical detection of materials in atomic scale and extracting the depth profiles with the sensitivity comparable to sub-layer structure [22]. Probing these states can provide a great deal of information about the material. This can be accomplished with various techniques, such as optical absorption, electron spin resonance, x-ray absorption, x-ray scattering, and many others using synchrotron radiation [22].

2 Synchrotron Techniques

In order to study the structure of materials and expand our knowledge in many fields, the need for an experimental facility like synchrotron has significantly grown over the years. The discovery of synchrotron radiation in 1947, and the development of the storage rings, has affected condensed matter physics and many other fields significantly [23]. As it is a great source of photons with a broad range of energies varying from the infrared to hard x-rays, it enables performing many experiments using different techniques. In this chapter, after a brief background of synchrotron radiation, a few experimental techniques that are used in our study of materials are described.

With the discovery of x-rays in late 1895 by Wilhelm Röntgen, a whole new platform of possibilities was presented to the society, particularly in physics, chemistry and medicine [24]. Nowadays more than ever, the use of x-rays as a tool of research is not limited to physicists. The broad range of possibilities varies from the determination of the inner structure of cells and biological organisms, chemical compositions, to fabrication techniques.

The use of x-rays started when Röntgen was working with the cathode-ray tubes; however it was around the 1960s that rotating anode sources were introduced and the subject of brilliance gained a new perspective [23]. The process of producing an x-ray beam can be simply explained via an x-ray tube in which electrons are accelerated between the cathode and the anode. When the electrons hit the cathode, given their high energy, they will be decelerated by inelastic collisions with the target atoms, and if their energy is high enough, a continuous spectrum of x-rays will be produced. Also, these high energy electrons lead to excitation of core electrons from the cathode, and then the decay of the core holes emit x-rays [25]. But the energies of these x-rays depends on the material itself and is limited to a few energies. Over the years, the use of x-ray tubes has been decreasing in spectroscopy methods since the maximum brightness that they are able to produce is limited when compared to synchrotron facilities, and therefore, much faster experiments can be carried out at synchrotrons. However, the benefit of using a synchrotron is not confined to brightness. Features

like tunability, polarization properties and spot size are a few additional advantages of using these facilities.

There are more than fifty synchrotron facilities working or under construction worldwide, making a lot of users able to perform various types of research. X-rays are a very useful tool for investigating the properties of materials for several reasons, one of which is the ability to probe into solid materials in a non-destructive manner. Additionally depending on their energy and electron density of the samples, the depth of probing can change [26].

Each synchrotron facility has an evacuated storage ring with high energy electrons circulating at high velocities. Beamlines which use the light emitted by the electrons are positioned tangential to their orbital path at spots that are defined by bending magnets and insertion devices [23].

Inside a storage ring, electrons that are previously accelerated to a desired energy by a booster ring are stored. Since the electrons will otherwise travel in a straight line, an external magnetic field is required to bend them according to the Lorentz force;

$$\mathbf{F} = q(\mathbf{E} + \mathbf{v} \times \mathbf{B}), \tag{2.1}$$

where q is the particle's charge, E is the electric field, $\mathbf{v}$ is the particle's velocity and $\mathbf{B}$ is the magnetic field.

The radiation produced due to this force is emitted in the direction of motion of the particles and then within the bending magnet, as the electron changes direction, a radiation beam between the new and the original electron direction is emitted. Thus, insertion devices such as undulators are placed between the bending magnets where the electrons travel on a straight path without the formation of radiation. An undulator will periodically deflect the electron beam using weak magnetic fields, which varying these magnetic fields will shift the resonance wavelength [25].

A synchrotron facility accessible in Canada, where we conducted our experiments, is the Canadian Light Source (CLS). It is located on the grounds of the University of Saskatchewan in Saskatoon, which is approximately the size of a football field and uses a third-generation 2.9GeV storage ring [27]. See Figure 2.1. The CLS was opened in 2004 and has expanded in many aspects since then, hosting scientists from all over Canada and around 20 other countries [27].

There are many synchrotron based spectroscopic techniques, X-ray absorption spectroscopies

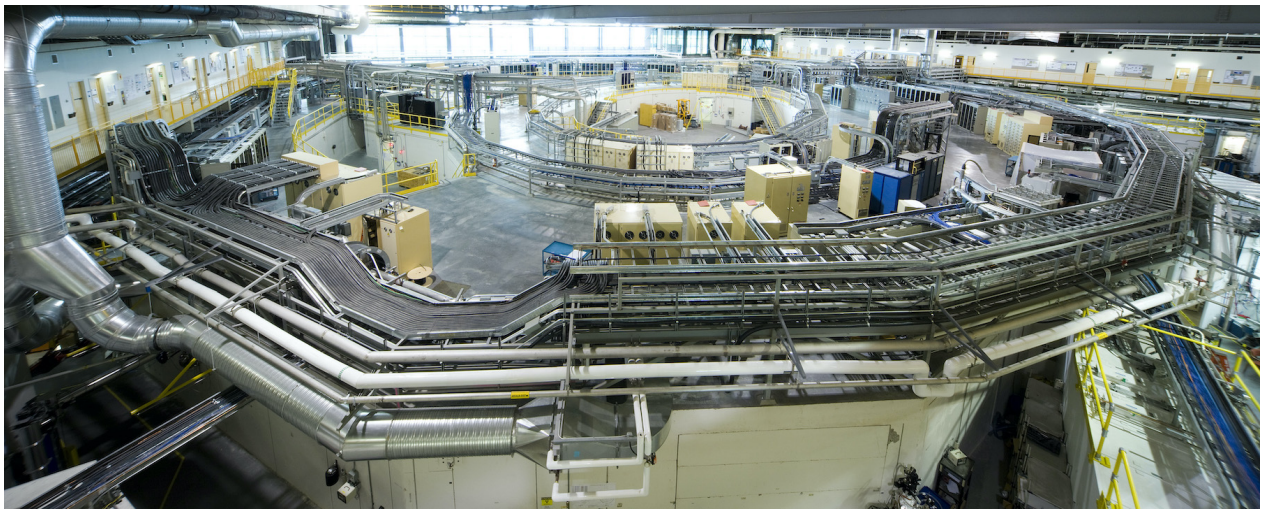

(a) CLS booster and storage rings inside the experimental hall

(b) CLS top view

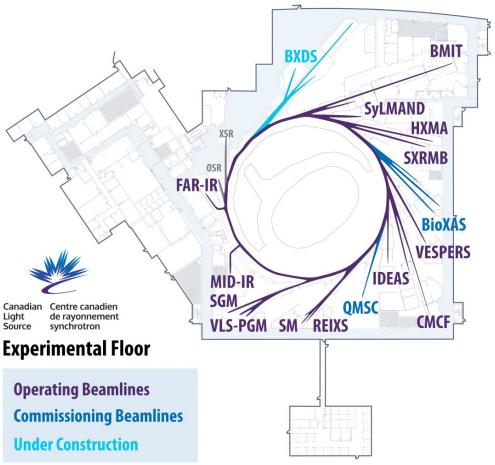

(c) CLS beamlines

Figure 2.1: (a) shows the Canadian Light Source storage ring (b) Shows the CLS located in Saskatoon, Saskatchewan (c) is a schematic of The CLS beamlines, Our data mostly was gathered from VLS-PGM and REIX. Images reproduced from [27].

(XAS) investigate how a material absorbs x-rays as a function of their energy. Generally, upon absorption of an x-ray an electron can be excited to an unoccupied state or gets ejected and is set free of its original atom's influence. Naturally these states relax by the emission of a photon or being scattered by neighbouring atoms or may even be leading to the ejection of photoelectrons, Auger electrons, and low energy secondary electrons. In effect, XAS probes the unoccupied states of the system [25]. In contrast, x-ray photoelectron spectroscopies (XPS) involves the collection and measurement of the energies of directly ejected electrons, yielding information about the core or valence state from which the electrons originated [28]. Hence, each point in an XAS spectrum

includes all of the possible processes taking place right after the absorption associated with a photon of a particular energy, and can, therefore, be viewed as the energy-integrated intensity of an XPS spectrum captured using the photon energy of that point in the XAS spectrum [25].

The information obtained by the wide available palette of synchrotron-based spectroscopies is interlinked. Since both the x-ray fluorescence and photoelectron spectroscopy rely on the absorption of x-rays, there is a direct correlation between them and absorption spectroscopy [25].

2.1 X-ray Absorption

X-ray Absorption Spectroscopy (XAS) has come a long way since its first appearance about a hundred years ago. This technique was developed by a few driven scientists at the time, in which there was not any possibility of practical application or a solid theory to explain the experimental observations precisely [29]. With Sayers, Stern and Lytle applying Fourier analysis to the point-scattering theory of x-ray absorption fine structure, for the first time, the ability to quantitatively determine structural parameters, such as the bond distance, coordination number, as well as the thermal and disorder parameters was made possible [29]. Following this ground-breaking progress, this method has progressed so much that nowadays, XAS can be a characterization tool in many fields such as materials science, solid-state physics and chemistry, etc [29]. There are many reasons for XAS to have such a significant impact, one of which is the existence of solid theory that renders the quantitative analysis of the XAS spectra possible. The increased possibility of collecting high-quality spectra at synchrotron facilities and the improvement of the data analysis process by reliable codes are also of great achievements. X-ray spectroscopy is correlated with the interaction of x-ray and matter. The photoelectric effect, which also occurs in UV radiation, plays a significant role in this interaction. When photons from an x-ray hit electrons of a metal, regardless of their radiation intensity, if they have enough energy, they will be able to remove electrons from the material. The minimum energy needed, which is the energy separation between the Fermi level of the material and the vacuum level, is called the work function of the metal, ϕ. When the photon energy is higher than the metals work function, the electron ejection will be accompanied by a kinetic energy on the order of the difference between the incoming photons energy and the work function [25].

The transition between an initial state Φ_i to the final state (the excited state, Φ_f) is governed

by the golden rule which the probability of this transition can be written as [30]:

$$W_{fi} = \frac{2\pi}{\hbar} | < \Phi_f | T | \Phi_i > |^2 \delta(Ef - E_i - \hbar\Omega) \tag{2.2}$$

where in this relation, the delta function δ will ensure the energy conservation and the transition will be possible if the energy of the final state, E_f, is equal to the sum of energy of the initial state E_i, and x-ray energy, $\hbar\Omega$.

This transition has a probability which is proportional to the photon flux, F_p [31]:

$$F_p = n\frac{\Omega^2}{\pi\hbar c^2} \tag{2.3}$$

in which n is the number of photons and Ω is the frequency of the x-ray beam. By dividing the transition probability W_{fi} by photon flux F_p one can get the X-ray absorption cross section as [31]:

$$\sigma = \frac{W_{fi}}{F_p} = \frac{4\pi^2\Omega}{3c} S\delta(E_f - E_i - \hbar\Omega), \tag{2.4}$$

in which the cross section area σ is given in m^2. In the case of an atom, the wave functions can be given J and M quantum numbers. The matrix element can be separated into a radial and an angular part. S is the radial matrix element and defines the line strength of a transition. The relation between cross section and penetration depth, λ_p, of the x-rays can be expressed by [31]:

$$\lambda_p = \frac{1}{\rho\sigma} \tag{2.5}$$

Where ρ is the density of the system. From the penetration depth, we can define a useful parameter, i.e. attenuation length μ. The attention length is defined as the penetration depth where the light(x-ray) intensity will decrease by the factor of $1/e$ from its initial incident intensity value. This means that a 1-(1/e) portion of the x-ray is absorbed within an attenuation length. Saying this, soft x-rays (with energies below 1keV) have an attenuation length of less than 1μm. For this reason, materials need to be extremely thin to perform transmission-based XAS using soft x-rays.

From an experimental perspective, given the dependency of an XAS spectrum on the energy of

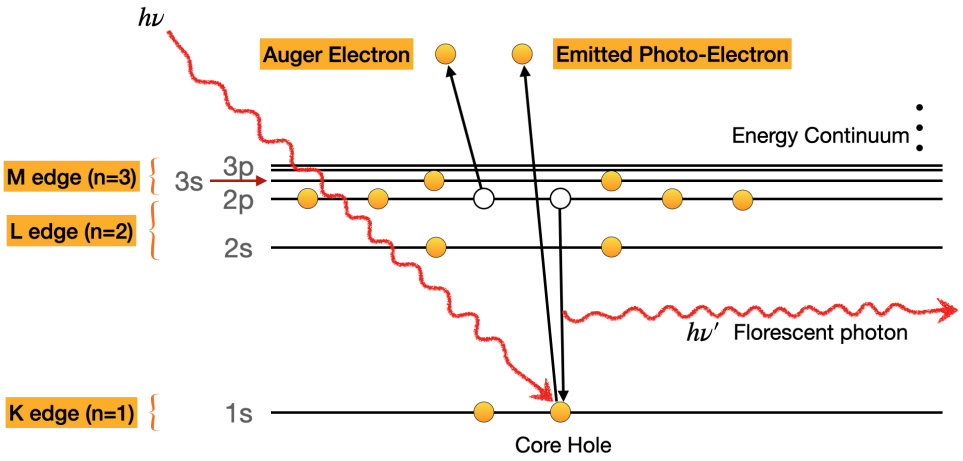

Figure 2.2: Scheme of the excitation and relaxation processes in X-ray absorption spectroscopy (XAS) and also the fundamental processes which contribute to XANES spectra are photoabsorption of an x-ray into a core level followed by photoelectron emission, followed by either filling of the core hole by an electron in another level, accompanied by fluorescence; **or** filling of the core hole by an electron in another level followed by emission of an Auger electron. Image based on reference [32].

the incoming beam, during an experiment, the x-ray energy needs to be able to change. This leads to using of a monochromator, which filters the desired wavelength from the radiation generated by a synchrotron. After passing through the monochromator, the intensity of the beam needs to be measured, which is usually performed via an ionization chamber for hard x-rays or a highly transparent gold mesh for soft x-rays which is done by monitoring the current just like in a total electron yield XAS measurement. This process is repeated after the beam interacts with the sample [31].

In XAS, the amount of x-ray absorbed by a sample, the difference between the initial intensity of the beam and the intensity of the transmitted beam is measured. Depending on the sample's composition, at specific energies, there will be a sharp rise in the absorption, which is called the absorption edge. At the absorption edge, the photon energy is equal to the binding energy of a core level, so these absorption edges can help determine the transitions from a ground state to a lower empty state [31]. If we consider an very thin layer of the desired material with the thickness of dl, while the initial intensity of the incoming beam I_0 is passing through the sample, it will lose dI of

its initial intensity value, in the following form of [31]:

$$dI = -\mu I_0.dl \tag{2.6}$$

here μ is a constant called the linear absorption coefficient with the combined effects of photoelectric and scattering processes.

The first x-ray absorption spectra were observed by de Broglie in 1913. He used a recording barometer with a single crystal mounted on its cylinder and rotated the crystal around its vertical axis at a constant angular speed so that as the crystal rotated [29], the x-ray was scattered at all the possible angles and thus according to the Bragg law:

$$2d \sin\theta = n\lambda \tag{2.7}$$

where θ is the angle between the incident beam and the layer's surface, d is the distance between the reflective surfaces, and n is the refractive index of the crystal. The x-ray energy changed and was recorded on a photographic plate. While examining the film, de Broglie found two distinct discontinuities, which proved to be the K-edge absorption spectra of silver and bromine atoms [29]. Of course, with the short wavelength and poor spectrographic dispersion, his spectra had low energy resolution and unable to resolve the fine structure. Nevertheless, his work had a remarkable impact on the development of this method.

XAS, via Beer-Lambert law,

$$I(z) = I_0 e^{-\mu z}, \tag{2.8}$$

Where $I(z)$ is the intensity of the beam at the penetration depth z; measures the exponential decay of a beam of photons at specific energy through a sample. For instance, when the photon energy is close to the first binding energy of an atom of the sample, due to excitation from 1s to p-states in the conduction band, the spectrum will feature a K-edge, and the other states will not contribute to the spectrum. The edges are, in part, named by which core electron is excited: the principal quantum numbers n = 1, 2, and 3 correspond to the K-, L-, and M-edges, respectively [33].

As each system begins with an initial state leading to a final state in XAS, absorption from an initial core level that has a defined symmetry moves to its final unoccupied state based on quantum

selection rules which are usually a mixture of components all based on the fact that XAS is sensitive to the local structure, it ends up being an excellent tool for various studies of amorphous solids, doped or ion-implanted materials, etc. [34].

XAS is also a powerful tool for studying correlated oxides when tuning the x-ray energies to the L2,3 edges of transition metal elements since this tuning leads to strong absorption resonances and the spectra can provide information about local orbital occupation, magnetism and spin state among many others []. This information can help in better understanding the effects of orbital and spin degrees of freedom in macroscopic properties.

X-ray Absorption Near Edge Structure (XANES), also known as near-edge X-ray Absorption Fine Structure (XAFS), is a type of absorption spectroscopy that focuses on the spectral features within 10-20 eV of the edge threshold. These features carry information about the local electronic structure of the absorbing atom [32, 35]. The central phenomenon in the XANES, similar to XAS, is the absorption of x-ray photons by materials that result in forming many-body excited states due to a core hole in a selected atomic level. With the single-particle theory approximation, the final state of this system is characterized by a core hole in the atomic core level and an excited photoelectron. As the core hole has a very short lifetime and the excited photoelectron, a short mean free path, the final state has a short lifetime. The core hole will be filled with an electron which later results in the emission of a fluorescent photon. In contrast to traditional photoemission experiments, in XANES in addition to the initial photoelectron, this fluorescent photon, Auger electron or a scattered photoelectron may as well be measured [35]. This affects the fact that in XANES, the final state of the photoelectron which does not need to be measured itself can be a bound state. This method can measure the total joint density of states of the initial core level with all final states while the conservation rules are preserved [32].

The great power of XANES is because of its elemental specificity [36]. Because the various elements have different core level energies, XANES permits extraction of the signal from a surface monolayer or even a single buried layer in the presence of a considerable background signal [36]. Buried layers are critical in engineering applications, such as magnetic recording media buried beneath a surface lubricant or dopants below an electrode in an integrated circuit. Because XANES can also determine the chemical state of elements that are present in bulk in minute quantities, it has

found widespread use in environmental chemistry and geochemistry. The ability of XANES to study buried atoms is due to its integration overall final states, including inelastically scattered electrons, as opposed to photoemission and Auger spectroscopy, which study atoms only with a layer or two of the surface. A lot of chemical information can be extracted from the XANES region: formal valence (challenging to determine in a nondestructive way experimentally); coordination environment (e.g., octahedral, tetrahedral coordination) and subtle geometrical distortions of it [36]. Transitions to bound vacant states just above the Fermi level can be seen. Thus XANES spectra can be used as a probe of the unoccupied band structure of a material [36].

2.2 X-ray Reflectometry

X-ray reflectometry is one of the main techniques for characterizing thin films and multilayers. From the optical point of view, an interface is defined by the change of refractive index through space. In the x-ray range, due to the small wavelength, a slight change in refractive index will introduce an interface, allowing x-ray waves to be reflected. The lost energy or momentum will indicate the intrinsic excitation and internal structure of the desired sample, and thus reflectometry helps retrieve this information [34].

The high interface sensitivity provided by reflectivity allows one to accurately determine the structural properties of heterostructures such as layer thicknesses and interface roughnesses by x-ray reflectivity. Recently, with the development of synchrotron radiation, the availability of photon sources with high brightness and tunable energy has opened new possibilities for x-ray reflectivity techniques to study additional properties apart from the structure.

If the energy of the incident photons is chosen in a manner, so it resonates with one of the absorption edges of the material, the method would be a resonant technique, and this would enhance the scattering cross-section of the material by a great deal. Electronic properties, for example, can be studied by tuning the x-ray photon energies to an absorption region[37, 22]. At these resonant frequencies, the refractive index depends highly on the valence shell properties of the resonant scattering centres and thus, the sensitivity to spatial variations of the electronic properties is dramatically enhanced. This makes Resonant X-ray Reflectivity (RXR) an ideal tool to study electronic structures at surfaces and lower layers in a non-destructive way. RXR is an element-

and interface-specific technique, which can provide enough data for electronic reconstruction by directly probing the electrons in the valence band in the transition metal across the interface. It is non-destructive, meaning that it does not alter the oxygen or the general chemical structure of the material. Since RXR is a relatively new technique, its full potential has yet to be reached.

In this method, as mentioned, by tuning the energy to the absorption edges of the different constituent of material, even in the same chemical element, if various sites have different chemical bondings or valances, different types of information can be obtained. Also, by tuning to different K, L or M edges of the same chemical element, one can get various information on electronic excitations of the materials under study.

While studying thin films and semiconducting materials in solid-state physics, which includes investigation of ultrathin layers, (which are of a thickness of a few nanometers), the visible light cannot be used to determine the interface patterns, thus here x-rays which have smaller wavelength can be utilized [38]. In terms of x-ray, the complex refractive index is slightly less than one and is given by[39]:

$$\tilde{n} = 1 - \delta + i\beta \tag{2.9}$$

where δ is dispersion, and β is absorption.

X-ray reflectometry (XRR) is a non-destructive synchrotron technique performed by measuring the x-ray intensity reflected from a surface, thin-film, and interfaces, as a function of the grazing incidence angle.it is widely used for its ability to determine the exact roughness, thickness, and density profiles of the desired sample in a non-destructive manner. This method can measure the above properties in a range of 1 to 500 nm, by setting the limits via the maximum recorded angle and the incident beam in the perpendicular plane to the sample [38].

In principle the fundamental building block of using x-rays reflectometry as a depth profiling method, follows the well-known Laue equations which if satisfied in three dimensions will form the receprical lattice [40]:

$$\mathbf{a_1}.\mathbf{\Delta k} = 2\pi k \tag{2.10a}$$

$$\mathbf{a_2}.\mathbf{\Delta k} = 2\pi h \tag{2.10b}$$

$$\mathbf{a_3}.\mathbf{\Delta k} = 2\pi l, \tag{2.10c}$$

Where k, h, l are the 3 Miller indices, and a_1, a_2, a_3 are the primitive vectors of the crystal lattice. Each choice of the 3 Miller indices, determines a scattering vector $\mathbf{\Delta k}$. Hence there are infinitely many scattering vectors that satisfy the Laue equations. They form a lattice, called the reciprocal lattice of the crystal lattice. This condition allows a single incident beam to be diffracted in infinitely many directions. However, the beams that correspond to high Miller indices are feeble and cannot be observed. These equations are enough to find a basis of the reciprocal lattice, from which the crystal lattice can be determined. This is the principle of x-ray crystallography [40]. In simple words, when the reciprocal lattice vector, $\mathbf{\Delta k}$, is equal to the momentum transfer, one can get a constructive interface. Depending on the properties of the waves interfering with each other, like amplitude and intensity, the strength of the interface and the intensity of the reflected wave will change. However, if one wave has a significantly larger intensity than the other, the amplitude will not vary that much since its also a function of incident angle and momentum transfer [38]. There are some conditions that can be applied in order to have a reflected wave with higher intensity, such as incidence at grazing angles, and when the refractive index between two areas of the interface is larger.

From an experimental point of view, an x-ray beam with wavelength λ, after passing through the monochromator (which filters the incoming x-ray beam to the desired wavelength), hits a sample at a grazing angle of θ. The reflected intensity is recorded via a detector at the angle of 2θ. This process is therefore called a $\theta/2\theta$ mode [38].

As mentioned, different refractive indices in different materials, which relate to different electron densities, result in reflection at the surface and interfaces. In case of having an incident angle θ, below a critical angle θ_c, we have a total external reflection, in which the density of the material can be determined from that critical angle. On the other hand, at angles above θ_c, the x-ray beam can penetrate inside the sample. In this case, for thin films, we have reflections at the top and the lower surfaces of the film. These reflected rays interfere and form interference fringes (regardless of their frequency).

Using a linear fit of squared incident angle of the beam θ^2, and squared Nth interference maxima

n^2, in the following form of [41, 39]:

$$\theta^2 = (\frac{\lambda}{2d})^2 n^2 + \theta_c^2, \tag{2.11}$$

where d is the thickness of the layer. Using the phase difference that occurs at the interface between the film and the substrate, and the difference between two neighbouring maxima and minima the thickness can be determined by:

$$d \approx \frac{\lambda}{2} \frac{1}{\sqrt{\theta_{n+1} - \theta_c^2} - \sqrt{\theta_n^2 - \theta_c^2}} \tag{2.12a}$$

$$\approx \frac{\lambda}{2} \frac{1}{\theta_{n+1} - \theta_n}, \quad for \;\; \theta_m \gg \theta_c \tag{2.12b}$$

Another factor that needs to be considered is the polarization of the incoming light. For this purpose, as mentioned in chapter 1, one can use the Fresnel equations for the electrical field vectors, parallel or perpendicular to the scattering plane, which are determined via the incoming and outgoing vector planes.

There are complexities in finding a proper model to describe the reflectivity, the fact that the beams can be reflected many times, which results in a complex interface harder to analyze, and the strong reduction of Fresnel coefficients at rough interfaces are to name a few [38]. Based on the mentioned properties of reflectometry, we can categories some characteristic behaviours for the RXR method [42]:

RXR could be thought of as a bulk sensitive method. The penetration depth of resonant x-ray photons depends on the material and the scattering geometry, however for the soft x-ray region, the depth range is approximately 0.1 μm, and an order above for hard-x-ray region [42].

RXR is also an element and orbital sensitive method since it can provide different information about the same chemical element with different chemical bondings, valances or crystallographic positions. Also, by tuning to different x-ray edges of that same chemical element, it can provide information on the electronic excitations of a system [42].

XRR can be performed on a variety of samples, including amorphous or liquid materials. For crystalline materials, instead of probing the contrast in scattering from each atom, XRR will measure

the contrast in the average electron density [25]. In most XRR experiments, measurements start just below the critical angle for the total reflection, so typically samples can have dimensions ranging from a few mm to a few cms, with the possibility of extending the recorded reflectivity intensity up to 5 orders or more[25].

Based on recent studies RXR is known to be sensitive to changes in electronic structure as small as single atomic layers in thin films. It has been successfully applied to detect and quantify redox-induced electron liquids at buried interfaces and electronic reconstruction due to polar discontinuities [34].

Although RXR can be a tool for large probing depth and sub-nanometer resolution, its full potential has not been reached yet, due to difficulty in extracting quantitative information from complex patterns of reflectivity from the desired interface. With our method, which is discussed in later chapters, we will get a quantitative estimate of charge transfer between the interface of $LaAlO_3$ and $LaFeO_3$ [22].

2.3 X-ray Excited Optical Luminescence (XEOL)

X-ray Excited Optical Luminescence (XEOL) is an x-ray photon in/optical photon out technique. It describes the converting process of the x-ray energy absorbed by the system to optical photons, often involving multi-step cascade processes. XEOL is commonly used along with XANES, which is described earlier to provide site-specificity, which can help reveal the electronic structure as well as the optical properties of the system of interest [43]. It is possible to use the time structure of a synchrotron radiation source to study the decay dynamics of a system via various optical de-excitation pathways. This particular technique is called time-resolved x-ray excited optical luminescence [44].

XEOL is essentially an energy transfer event in which the absorption of the x-ray photon produces a large number of energetic electrons, both photoelectron and Auger [45]. These fast electrons, in turn, cause further ionization and excitation. The energy is transferred to luminescent centers through inelastic procedures, which leads to the creation of holes in the valence band as well as electrons in the conduction band of semiconductor nanostructures under study [45]. The recombination of holes and electrons will emit light, as the difference between the final and initial energies fall within visible light region.

Using laboratory soft x-rays such as Mg Ka (1263.6 eV) and Al Ka (1486.6 eV), and visible-UV and soft x-ray (20 eV 3 keV) from a tunable synchrotron light source (e.g. CLS), it is often possible to conduct site and depth selective measurements [44]. The sampling depth selectivity comes from the energy-dependent penetration depth of the photons, and the site selectivity comes from the tunability of the source [44]. For instance, if the photon energy is tuned to the carbon K- edge (1s), the photon can be preferentially absorbed by the carbon dioxide atom. This particular channel selective excitation will significantly facilitate the identification of the origin of luminescence. Soft x-ray photons are ideally suited for studies of thin films since their penetration depth, typically in the range of one absorption length (see section X-ray Absorption), is comparable to the standard thickness of thin films used in our studies. One-absorption length is the 1/e attenuation length of the incident photon [44].

Sensitive XEOL could be obtained by tuning the photon energy to the C, N and O K-edge or varius other elemental edges for elements in the samples. Further penetration depth selectivity can be obtained by varying the angle of incidence of the photon beam. The optical photons have attenuation lengths of the order of mm which means their reabsorption is not important for experiments or analysis [44].

The optical luminescence which is occasionally emitted following atomic, core level x-ray excitation has been suggested as a mode for detecting X-ray Absorption Near Edge Structure (XANES) since x-ray may provide further capabilities to XANES spectroscopy, and could include information that can not be obtainable by other experimental methods [46]. Particularly, the optical detection XANES could make available the wide-ranging capabilities for fast-time-scale counting. XEOL has been recommended as a means for obtaining site-specific information about an element in a multi-site sample [46]. Site-specific information will be obtained by observing an optical luminescence line that is uniquely resolvable due to the emitting ion's structural setting [46]. Site selectivity would provide an enormous advantage for XANES studies involving a wide range of problems, notably multicomponent sample that cannot be analysed with more conventional methods.

XEOL is mainly based on the process of luminescence, which is an emission of light, and there are many forms of this light emission. Photoluminescence a specific form of light emission in which photons from an x-ray beam interact with a sample, and after exciting the electrons to a higher energy state, this process is called photoexcitation, the relaxation to a lower energy state will

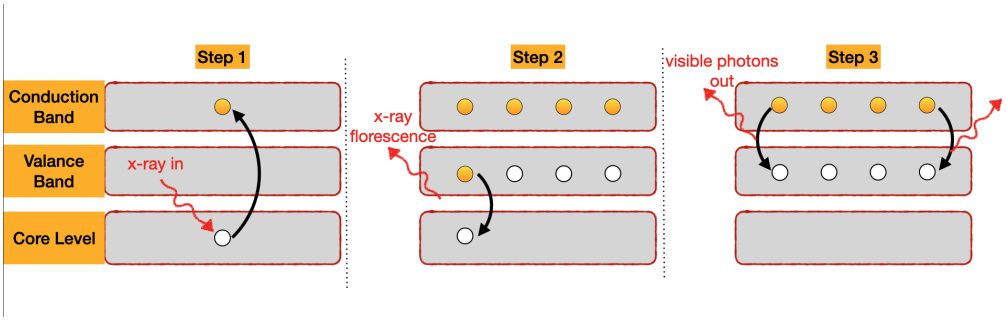

Figure 2.3: A schematic of the XEOL process in luminescent materials. Step 1 is creation of the core holes and more electrons in the conduct band, taking place within femtoseconds. In Step 2, the electrons from the valence band fill into the core hole with x-ray fluorescence or Auger decay which generates additional holes in the valence band. Step 2 is also ultra-fast process. In Step 3, the electrons in the conduction band and the holes in the valence band resulting from secondary processes recombine and generate optical luminescence [47]. Image reproduced from [47].

result in the emission of photons with higher wavelength, in the visible range [44]. Depending on the exact wavelength of the absorbed photon (in our case, the photons from x-ray beams), the excitation process might result in the occupation of different vibrational levels of the excited state. As these electronically excited states are unstable and naturally want to relax, they transit back to their initial state accompanied by different manners of dissipating energy. It is notable to mention that the process of relaxation can be in the form of a rapid vibrational relaxation, which essentially is a transition of the excited state into a vibrational state with lower excitation energy but of the same energy level. In this process, no energy is dissipated, and all of the initially absorbed energy is exerted in the form of heat. Therefore no emission of light will be detected [48]. In the relaxation processes that photons are re-radiated, the time period between absorption and emission may vary. Ranging from short femtosecond up to milliseconds and, in some particular cases, with a delayed emission up to minutes. In general, observing a photoluminescence effect at certain energy is an indicator of the transition energy associated with an electron occupying an excited state [44]. Since XEOL is focused on the de-excitation of a core-electron, we can use the yield of the optical photon as a function of excitation energy and get the luminescence specific to a particular decay of material. Or in other words, focus on the fingerprint of that particular desired characterization.

3 Synchrotron Analysis of $LaFeO_3$ and $LaTiO_3/LaFeO_3$ Heterostructures

3.1 Introduction

In this chapter, oxide heterostructures involving layers of the anti-ferromagnetic Mott-Hubbard insulator $LaTiO_3$ and layers of the anti-ferromagnetic charge transfer insulator $LaFeO_3$ are studied using synchrotron techniques. The synchrotron data was acquired by my supervisor prior to my studies, but the analysis was led by myself with direction from my supervisor. Previous works [6] have indicated that this interface may exhibit atomic-scale charge transfer, which is difficult to detect and characterise. Using a combination of XAS and RXR on several samples, the main goal is to quantify charge transfer at the interface and determine subsequent changes in magnetic properties driven by this charge transfer. It is noteworthy to say that controlling the number of transferred electrons and hence the properties of the interface, opens up new pathways to design optimal functioning oxide interfaces. Additionally, both bulk $LaFeO_3$ and bulk $LaTiO_3$ have a partially filled $3d$ transition metal ion on the B site. This suggests the opportunity to use the differences in band configuration of $LaTiO_3$ and $LaFeO_3$ near the Fermi level to drive electronic reconstruction.

3.1.1 Earlier Works

Several groups reported the formation of a nonmagnetic band insulator at the isopolar interface between the $LaTiO_3$ and the $LaFeO_3$. By density-functional theory calculations, they report the formation of this interface state is driven by the combination of O band alignment and crystal field splitting energy of the t_{2g} and e_g bands[6]. At $LaTiO_3/LaFeO_3$ interfaces, this competition results in both charge transfer and a rearrangement of the Fe bands which can lead to a new nonmagnetic band insulating state at the interface. Using in-situ x-ray photoelectron spectroscopy (XPS), they

([6]) confirmed the charge transfer and band rearrangement experimentally and determined an electron transfer up to 1.2 ± 0.2 e^- per interface unit cell in $LaTiO_3/LaFeO_3$ heterostructures. With focus on internal charge transfer, in $LaTiO_3/LaFeO_3$ heterostructures, alignment of the O bands is expected to occur at the interface, due to the two materials sharing their oxygen atoms at the interface. As a result of this band alignment, the empty upper $3d$ band of $LaFeO_3$ is expected to be pushed below the energy level of the partially filled lower $3d$ band of $LaTiO_3$, which would cause an electron transfer from Ti to Fe.

3.1.2 Concepts of Charge Transfer and Spin State

As mentioned earlier and in previous works, the main idea and focus of this particular interface is the charge transfer from $Fe^{3+}Ti^{3+}$ to $Fe^{2+}Ti^{4+}$. At the interface, the non-bonding oxygen bands of $LaTiO_3$ and $LaFeO_3$ align, the Ti $3d$ bands are empty, and 6 electrons are located in the Fe $3d$ band. This means that one electron is transferred from Ti to Fe, resulting in Ti^{4+} and Fe^{2+}. In addition, a rearrangement of the Fe $3d$ bands in the $LaTiO_3/LaFeO_3$ heterostructure is observed. Spin state refers to the potential spin configurations of the central metal's d electrons in description of transition metal coordination complexes. In various cases these spin states vary between high-spin and low-spin configurations. These configurations can be understood through the two major models used to describe these coordination complexes; crystal field theory which describes the breaking of degeneracies of electron orbital states, and ligand field theory, which is a more advanced approach similar to molecular orbital theory[49]. In order for a low-spin configuration to occur, the energy cost of placing an electron into an already singly occupied orbital must be less than the cost of placing the additional electron into another orbital at an energy cost of Δ. If the energy required to pair two electrons is more than Δ, a high spin configuration, or a rearrangement of the Fe $3d$ bands occurs. A high-spin to low-spin transition makes this rearrangement, which is a result of the competition between Hund's exchange and crystal field splitting. Typically for Fe^{2+}, the high-spin state is favorable. But due to the relatively large crystal field splitting in $LaFeO_3$, after the charge transfer to stabilize a Fe^{2+} configuration, the Fe might exist in a less common low-spin state. As a result, the strong electron transfer observed at the $LaTiO_3/LaFeO_3$ interface may be accompanied by a loss of magnetic moment. Both high spin and low spin states are possible in octahedral complexes. However, in tetrahedral metal complexes with small crystal field splitting, the energy

required to pair up the spins is always higher than the amount of energy needed to transfer between energy orbital splittings. See Figure 3.1 for a depiction of the high spin and low spin configurations for Fe^{2+}.

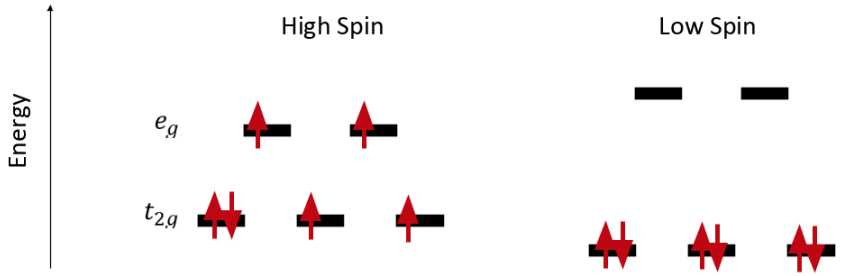

Figure 3.1: A schematic of relative energies regarding the high spin states in octahedral metal complexes with weaker crystal field splitting (left)and low spin states in octahedral complexes with larger crystal field splitting (right). The e_g orbitals refer to the transition metal $d_{x^2-y^2}$ and $d_{3z^2-r^2}$, while the t_{2g} are the d_{xy}, d_{xz}, and d_{yz}.

3.2 Experimental details

Our $LaTiO_3/LaFeO_3$ study consists of three samples grown by collaborators using pulsed laser deposition (PLD). Existing reflectivity and XAS data were measured by Prof. Green at an experiment temperature of 200 K to avoid radiation damage. XAS and resonant x-ray reflectometry (RXR) experiments have been performed at the Resonant Elastic and Inelastic X-ray Scattering (REIXS) beamline of the Canadian Light Source (Saskatoon, Canada), using linearly σ and π polarised light. Analysed measurements were performed with following conditions: XAS [total electron yield (TEY), total fluorescence yield (TFY)] and fixed Q reflectivity with linear vertical (LV, σ) and linear horizontal (LH, π) polarisation and Fe $L_{2,3}$, Ti $L_{2,3}$, O K, and La $M_{4,5}$ edges. Theta-2Theta reflectivity at fixed energy measurements were performed using non-resonant energies for structural information (400 - 900 eV) (LV only) and resonant energies at several points over all aforementioned edges (both LV and LH polarisations). Each sample has the same $LaAlO_3$ capping and bulk $SrTiO_3$ substrate, but different thicknesses of $LaTiO_3$ and $LaFeO_3$ layer as shown in Figure 3.2.

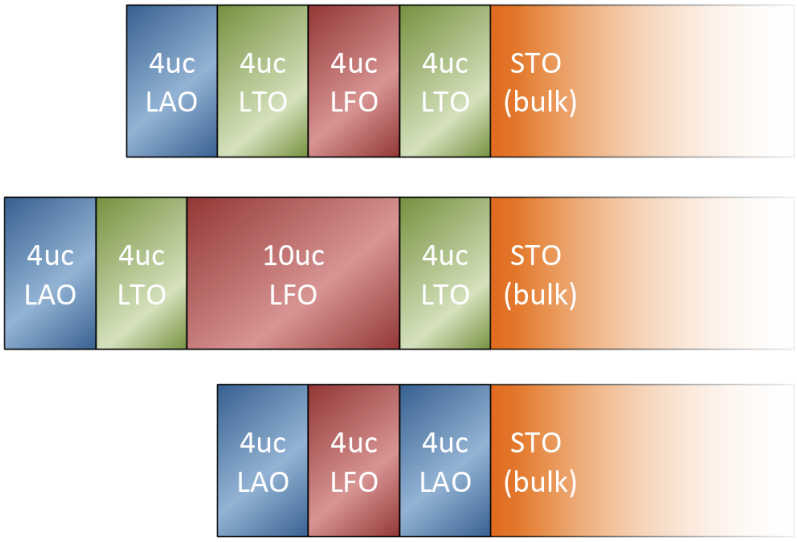

Figure 3.2: A schematic of the different heterostructures studied for this project. In this schematic uc stands for unit cell, LAO, LFO, LTO, STO are short for $LaAlO_3$, $LaFeO_3$, $LaTiO_3$, $SrTiO_3$, respectively.

3.3 The Model Used for RXR Analysis

Reflectivity modelling is done using QUAD [50] and Quanty [51] programs on University of Saskatchewan's cluster computers (Plato). Based on RXR data, the sequence of steps to perform is as follows: first, a model was set up consisting of a sequence of layers k containing elements (in their respective valence) i, with the parameters being the thickness t_k, atomic concentration $c_{i,k}$ and roughness of the respective upper interface $\sigma_{i,k}$. We then simulate the resulting RXR curves using QUAD, compare them with the measured curves and optimise the parameters until convergence is achieved. The initial layer sequence depends on the complexity of the system and reflects preliminary information about surfactant layers, intermixing regions and so on. From the parameters of the individual layers t_k, $c_{i,k}$ and $\sigma_{i,k}$, we obtain the elemental depth concentration profiles $c_i(z)$ of the entire heterostructure. Properties are described by atomic scattering factors $f_i(\omega)$ with a unique photon frequency dependence, which we derive from the XAS spectra.

Writing refractive index n in terms of relative permittivity ϵ_r, and relative permeability μ_r,

$$n = \sqrt{\epsilon_r \mu_r} \tag{3.1}$$

and recalling the relation of relative permittivity to susceptibility χ, as:

$$\chi = \epsilon_r - 1, \tag{3.2}$$

the elastic response of the entire heterostructure can be described by the depth-resolved susceptibility formula [4]:

$$\chi(z,\omega) = \frac{4\pi}{|\mathbf{k_0}|^2} r_{el} \sum_i N_A c_i(z) f_i(\omega) \tag{3.3}$$

where $\mathbf{k_0}$ is the wave vector of the incoming beam, r_{el} is the classical electron radius and N_A is the Avogadro number. On the basis of $\chi(z,\omega)$, RXR spectra can be simulated using the Parratt formalism [22]. Finally, using the built-in features of QUAD, a non-linear least squares algorithm is used to optimise χ^2, the deviation between the measured data and the simulated spectra. From the atomic scattering factors we could calculate the dielectric tensor ϵ and the refractive index $n(\omega) = 1 - \delta(\omega) + i\beta(\omega)$ of the film. The XAS measurements were carried out in the total electron yield (TEY) mode.

3.3.1 Fitting function and Algorithm

As mentioned for the fitting process we used a non linear least square algorithm. In this section there will be a short description of the algorithm. We used a non-linear least squares which is a form of least squares analysis used to fit a set of data with a model that is non-linear in a number of parameters. This method is based on making an approximation by a linear model and then refining the parameters by successive iterations.

By finding initial parameter estimates that are close to the ideal values, the problems with divergence can be simplified by a simulation. The initial parameters of the model are adjusted manually until there is an acceptable agreement between the observed and calculated data thus creating a good starting point for the non-linear refinement, and to reduce the chance of optimizing toward a local minimum in χ. Using algorithms significantly boosts the process of initial estimate and creates a solution for the curve fitting problem.

A suitable algorithm to solve non-linear least squares problems that mostly arise in the least squares curve fitting is the Levenberg-Marquardt algorithm. This algorithm which was first pub-

lished in 1944 by Kenneth Levenberg and later rediscovered in 1963 by Donald Marquardt, like other numeric minimization algorithms is an iterative procedure. QUAD uses the Levenberg-Marquardt algorithm, as implemented in the library levmar (http://users.ics.forth.gr/ lourakis/levmar/).

3.4 RXR Results for the $LaAlO_3/LaFeO_3$ Heterostructure

In this section, the RXR analysis results for the $LaAlO_3/LaFeO_3$ heterostructure (i.e. the bottom sample of Figure 3.2), are demonstrated. The results consist of resonant and non resonant reflected intensity at both fixed momentum transfer and varying energy and fixed energy with varying momentum transfer. A table of the fitted parameter values which are extracted from the fitting is also presented.

The RXR fitting starts with general refinements of the assumed structure of the material, using the non-resonant fixed energy data, where the theta and two-theta reflection angles are scanned. The non-resonant results are shown in Figure 3.3, where both the experimental data and fitted results are shown. As it is shown in the Figure 3.3 for the experiments, a range of energies were used and fitted as the momentum transfer varies. In the process of fitting the general thickness and roughness was refined for every layer. Also the fitting took into account the thickness, roughness and density parameters of the surface contamination.

The second step of the RXR fitting is to now include the resonant fixed energy scans, which allows a more precise fitting of the elemental concentration profiles, and allows different valences to be considered in the fitting. Since $LaFeO_3$ has only Fe^{3+} in bulk form, we assumed the $LaFeO_3$ layer would be trivalent as well, but allowed for interface charge transfer, including the possibility of Fe^{2+} at both interfaces to the $LaAlO_3$. Additionally, we found that we need to include the possibility of Ti^{3+} at the interface to the $SrTiO_3$, which only has Ti^{4+} in bulk. After allowing these different valences in the fitting, and including both the resonant fixed energy scans as well as fixed momentum transfer scans for the Fe and Ti resonances, we were able to significantly improve the quality of the fit. The resonant fixed energy scans are shown in Figure 3.4. In this process the energies of near Ti L_3, Fe L_3 and La M_5 resonances were used to get the fringes in which for each set of curves the sensitivity to each relevant elements properties can be observed. The curves with energies near Ti and Fe resonances are sensitive to any change in Ti and Fe valances, while the

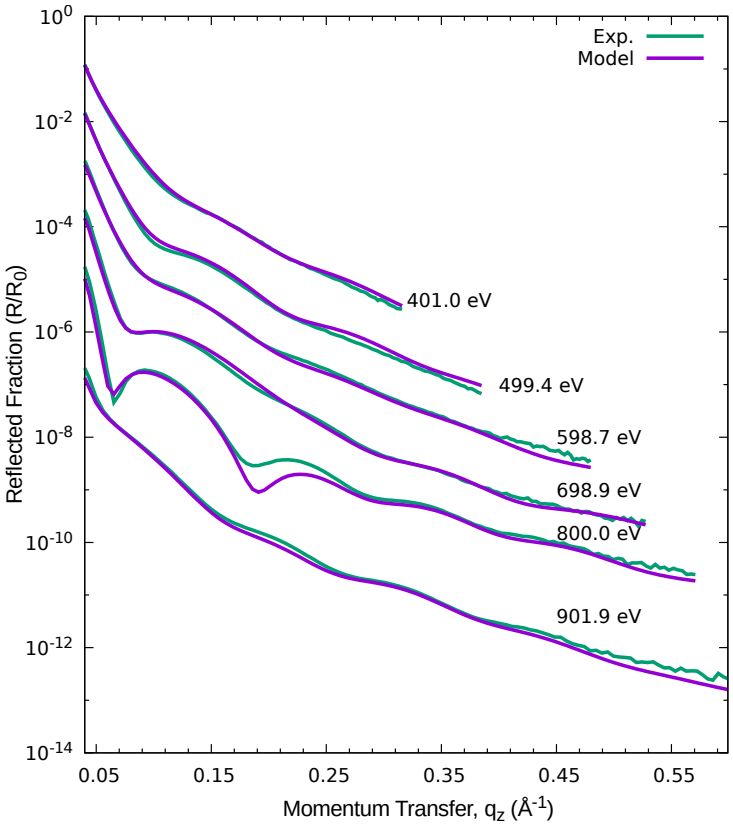

Figure 3.3: Non-resonant, fixed energy RXR for the LAO/LFO/LAO/STO heterostructure. Experimental data is shown along with the fitted model results. For each pair of curves, the photon energy is shown on the plot. Curves are offset vertically for clarity.

curves with energies near La resonances are sensitive to the roughness and thickness of the La.

The fixed momentum transfer scans across the Fe $L_{2,3}$ resonance are shown in Figure 3.5. Here, only σ polarization scans were analyzed, as the π polarization scans were similar. The top curves of the Figure which have the lowest momentum transfer are the result of grazing incidence angles and are very similar to the typical XAS lineshape of Fe^{3+} and higher momentum transfers are shown in the bottom curves. From having a good fit of model to the experimental data we can observe that there is no Fe^{2+} present, meaning there is no charge transfer to Fe. The lack of charge transfer here is expected considering that this material does not have $LaTiO_3$.

The fixed momentum transfer scans across the Ti $L_{2,3}$ resonance are shown in Figure 3.6. Here, both σ and π polarization scans were analyzed, as there are significant differences between them. the complex lineshapes of the curves are due to the existence of Ti^{3+} as well as Ti^{4+} [52]. based on

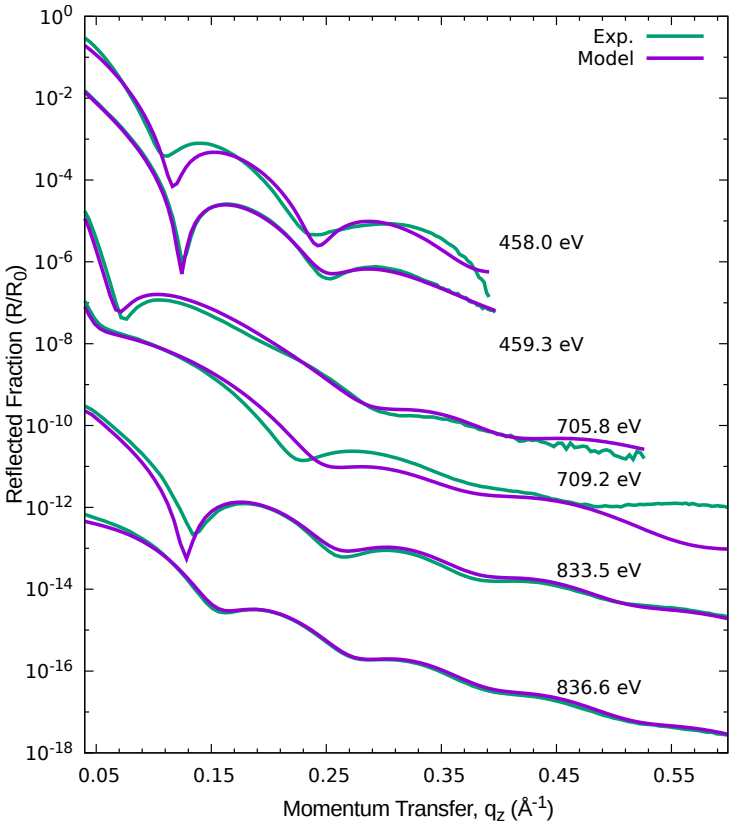

Figure 3.4: Resonant, fixed energy RXR for the LAO/LFO/LAO/STO heterostructure. Experimental data is shown along with the fitted model results. For each pair of curves, the photon energy is shown on the plot. The top two curves have energies near the Ti L_3 resonance, the middle two near the Fe L_3 resonance, and the bottom two near the La M_5 resonance. Curves are offset vertically for clarity.

the mentioned article, in the fitting process the Ti valances and orbital energies were allowed to fit. All the above lead to a vety good fit as shown in the Figure 3.6 for both σ and π polarization.

The results of the fitting are summarized in the structure plots shown in Figure 3.7. In the top panel, the concentration of anions throughout the structure are shown. This includes surface contamination (due to atmosphere exposure), as well as the oxygen atoms throughout the heterostructure. The bottom panel shows the perovskite A-site concentrations (La atoms in the films and Sr in the substrate). There it is visible that the interface between La and Sr has some roughness and intermixing, and the surface of the films has slightly less roughness than the interface. The middle panel of the Figure shows the concentrations and valences of the B-site atoms in the perovskite. Again, the surface layer has slightly less roughness than all of the interfaces, which

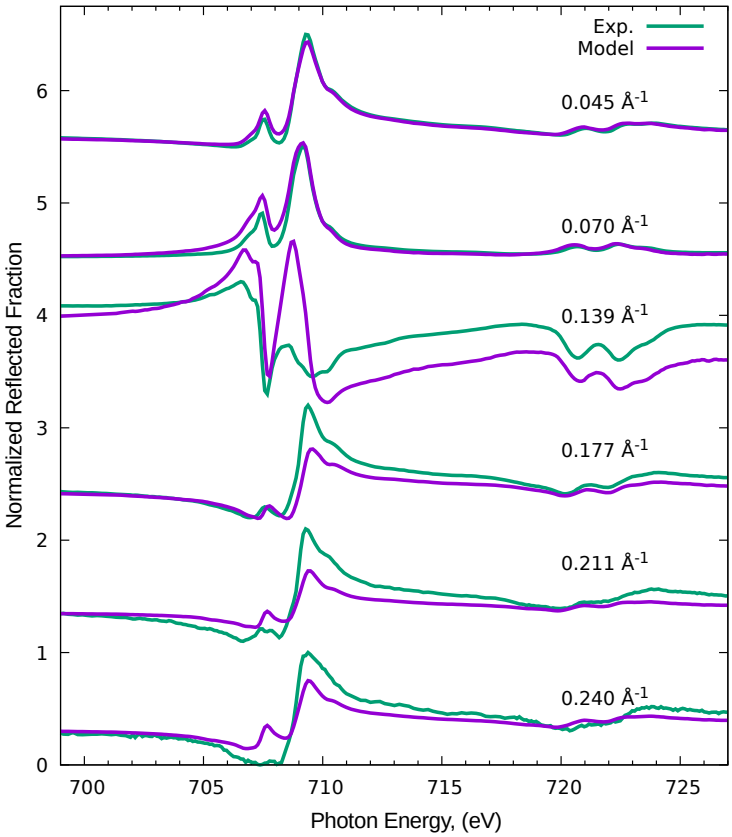

Figure 3.5: Resonant, fixed q_z RXR for the LAO/LFO/LAO/STO heterostructure, for energies spanning the Fe $L_{2,3}$ resonances. Experimental data is shown along with the fitted model results. For each pair of curves, the fixed momentum transfer value is shown on the plot. Curves are offset vertically for clarity.

indicates there is intermixing at the interfaces. Essentially all of the Fe is in the trivalent Fe^{3+} state, as was suggested by the Fe scans in Figure 3.5. There is some Ti^{3+} near the interface in the $SrTiO_3$. While this Ti valence change was not the topic of the project, it is interesting to see, and it is a result of the polar discontinuity at the interface to the $SrTiO_3$. Polar discontinuities will be discussed in more detail for the project in the next chapter.

The specific fitted roughness and thickness values are shown in Table 3.1. The uncertainty values are given by the QUAD program and come from the covariance matrix from the Levenberg-Marquardt fitting. As can be seen, the uncertainty values are quite small, which indicates the good sensitivity of RXR for this application. The film thicknesses are close to those expected from the growth, but the Fe is slightly thicker than the Al layers. Part of this is due to the smaller lattice

constant for $LaAlO_3$ compared $LaFeO_3$ (3.79 Åvs 3.96 Å). Additional fit parameters, like the Ti^{3+} concentration in the $SrTiO_3$ and the orbital energies of the Ti, are not included since they are not the focus of this project.

Table 3.1: Main parameters fitted for RXR model.

Parameter	**Thickness** (Å)	**Roughness** (Å)
Surface	4.58 ± 0.80	4.60 ± 0.34
Al_{upper}	12.17 ± 1.13	1.29 ± 1.21
Fe	17.65 ± 0.46	5.79 ± 0.12
Al_{lower}	11.54 ± 0.18	6.40 ± 0.13
Ti	-	9.27 ± 0.12
Sr	-	7.23 ± 0.23
La	48.03 ± 0.21	3.10 ± 0.08

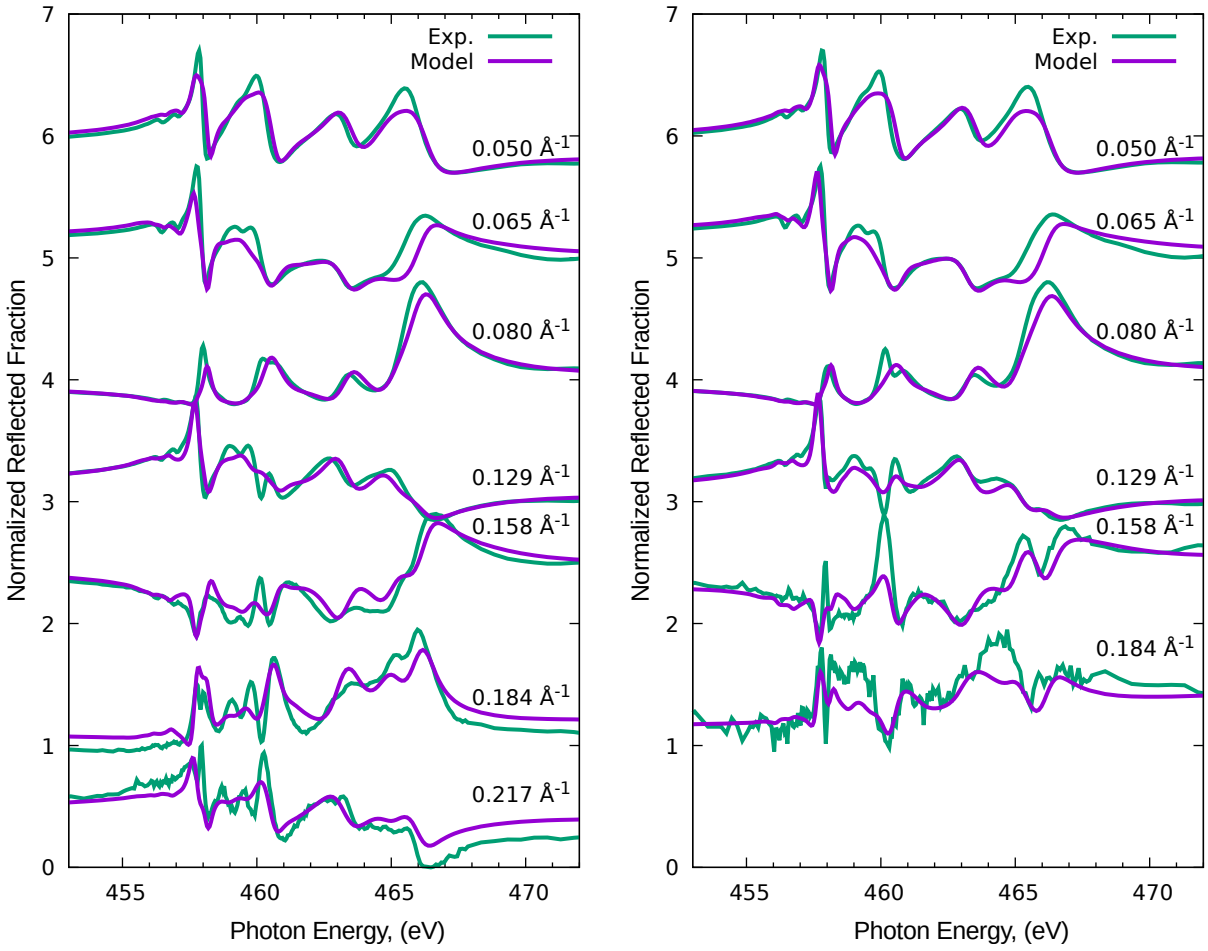

Figure 3.6: Resonant, fixed q_z RXR for the LAO/LFO/LAO/STO heterostructure, for energies spanning the Ti $L_{2,3}$ resonances. The left panel shows results with σ-polarized light, while the right panel shows π-polarized results. Experimental data is shown along with the fitted model results. For each pair of curves, the fixed momentum transfer value is shown on the plot. Curves are offset vertically for clarity.

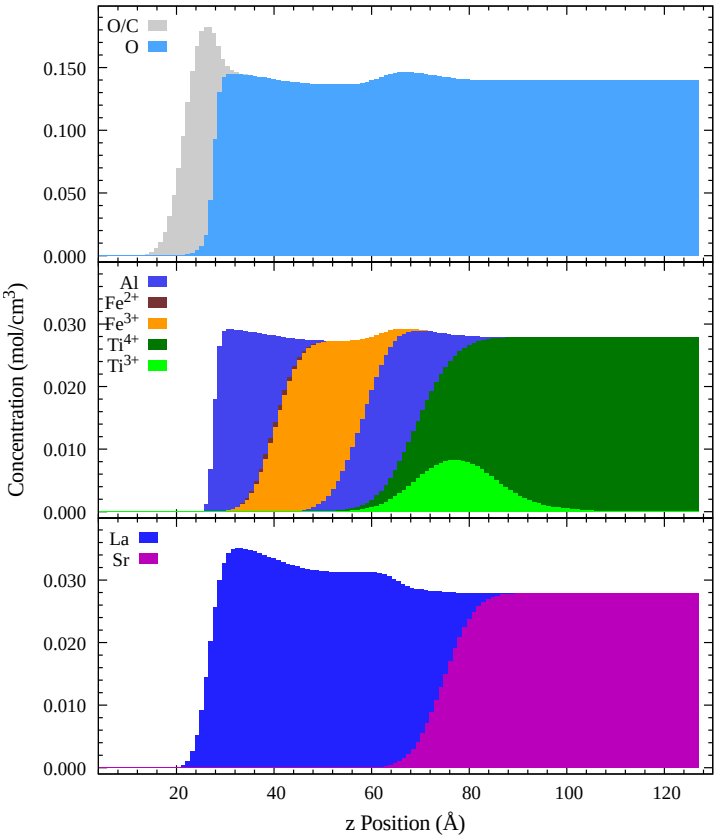

Figure 3.7: Elemental and valence concentration profiles of the LAO/LFO/LAO/STO heterostructure determined using RXR. The top panel shows anion (oxygen) density and organic surface contamination (carbon/oxygen). The middle panel shows the concentration of the perovskite B site atoms throughout the heterostructure, including the specific valences of Fe and Ti. The bottom panel shows the concentration of the A site atoms.

3.5 XAS Fitting Results

In this section the analysis results of XAS spectra of the Fe $L_{2,3}$ which were collected in TEY mode is presented. The main goal is to determine the charge transfer to Fe by using the Fe $L_{2,3}$ XAS spectra.

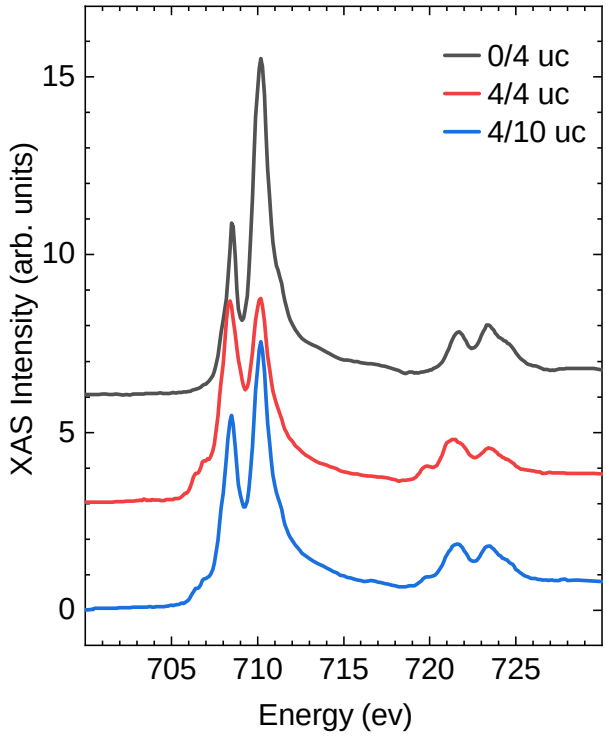

Figure 3.8: Experimental Fe $L_{2,3}$ XAS collected in TEY mode for the $LaTiO_3/LaFeO_3$ heterostructures. The spectra are labelled according to the thickness of the $LaTiO_3/LaFeO_3$ layers in the structure, in units of unit cells.

Figure 3.8 shows the experimental XAS spectra for the $LaTiO_3/LaFeO_3$ heterostructures illustrating the changes in XAS intensity as energy changes. There are two peaks at Fe edge which is indication that there is a varying mixture of Fe^{2+} and Fe^{3+} in the samples [30, 53].

In order to roughly quantify how much of each valence state was in each sample, we first used the spectral differences method to isolate Fe^{2+} and Fe^{3+} reference spectra for this system [53]. By comparison to Fe^{3+} in the literature, the sample with no $LaTiO_3$ appears to have entirely Fe^{3+} [30]. We cannot claim that there is absolutely no Fe^{2+}, but because of the lack of any features

in the pre-edge region, it appears the amount of Fe^{2+} in this sample would be below 5% at most. So the spectrum for the sample with no $LaTiO_3$ was used as our reference spectrum for Fe^{3+}. We then isolated the Fe^{2+} component by subtracting the Fe^{3+} reference from the 4/4 sample (4 unit cells in the layers of both $LaTiO_3$ and $LaFeO_3$). Similar to previous studies [53], we subtracted the largest amount of Fe^{3+} without creating any dips or otherwise atypical features in the resulting spectrum. With this approach we found that 50% of the spectrum for the 4/4 sample was from Fe^{3+}, and therefore the other 50% (by edge jump height) was from Fe^{2+} (by the appearance of atypical features, the uncertainty in this approach is roughly ±5%). The leftover spectrum then became our Fe^{2+} reference spectrum, and is very similar to other Fe^{2+} spectra found in oxides [54]. These two reference spectra, normalized by edge jump height, are shown in Figure 3.9.

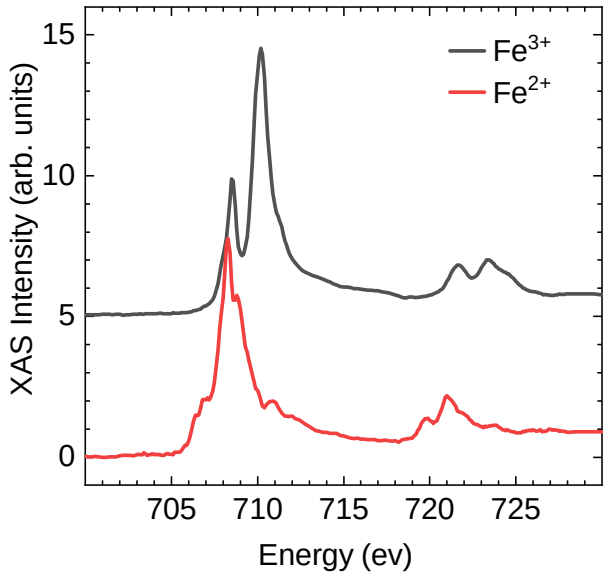

Figure 3.9: Fe $L_{2,3}$ XAS reference spectra of the two oxidation states, extracted from the experimental spectra of the two samples as discussed in the text.

We then fitted a combination of these two component spectra to the third sample, having 4 uc layers of $LaTiO_3$ and a 10uc layer of $LaFeO_3$. Using least squares fitting, we found this experimental spectrum was 34% Fe^{2+} and 66% Fe^{3+}. The Fe valence fractions are summarized in Table 3.2. As described above, the fractions for the 0/4 sample were obtained under the reasonable assumption that it is entirely Fe^{3+} within 5% error. The fractions for the 4/4 sample were determined by spectra differences and restricting to a reasonable resulting difference spectrum. The fractions for

the 4/10 sample were determined by least squares fitting using the component spectra. The major uncertainty comes from the systematic errors for the first two samples, and we estimate it to be ±5%.

Table 3.2: Valence fractions for the $LaTiO_3/LaFeO_3$ heterostructures extracted from XAS analysis. The samples are labelled according to the thicknesses of the $LaTiO_3/LaFeO_3$ layers in units of unit cells.

Sample	**Fe^{2+} Fraction**	**Fe^{3+} Fraction**
0/4	0.00 ± 0.05	1.00 ± 0.05
4/4	0.50 ± 0.05	0.50 ± 0.05
4/10	0.34 ± 0.05	0.66 ± 0.05

There is an important consideration to make since these spectra were collected in TEY mode, they only probe roughly 5-10 nm into the sample and will have a depth dependence to them. Since our thickest heterostructure has a thickness of roughly 8-9 nm, we likely do not probe the entire thickness of the film equally. So these extracted valence fractions should not be interpreted as an exact quantification of the charge on the Fe in the heterostructures. However, they can be used as a qualitative confirmation of the existence of charge transfer. The previous studies [6], found a charge transfer of 1.2 ± 0.2 electrons per square unit cell for the $LaTiO_3$ interfaces. For our 4/4 sample, our extracted valence fractions correspond to 1.0 ± 0.1 electrons per square unit cell. So we see a similar amount of charge transfer. For our 4/10 sample, the valence fractions correspond to 1.7 ± 0.3 electrons per unit cell. This is a bit larger than expected, but this is the thickest sample where our TEY analysis will have the largest possible error. However, overall we can conclude that with XAS we detect a similar amount of charge transfer. Additionally, our extracted Fe^{2+} spectrum can address the issue of the spin state of the charge transfer Fe state at the interface. Comparison with spectra in the literature [30, 54] show that this is clearly a high spin Fe^{2+} spectrum. So we find that the predictions of the non-magnetic band insulating state at the interface were incorrect. It appears the crystal field splitting in at the interface is not sufficient to stabilize the low spin state. This is an important result from our XAS analysis that was not possible via the earlier XPS studies.

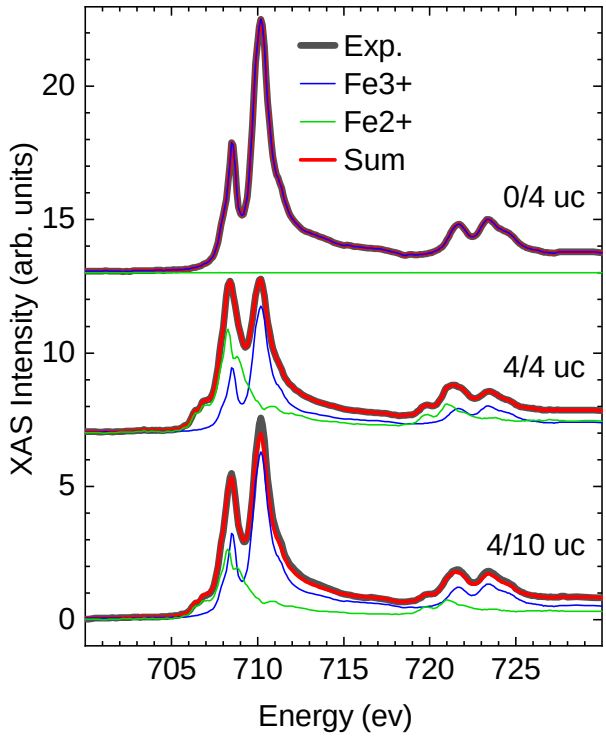

Figure 3.10: Decomposition of the Fe $L_{2,3}$ XAS spectra into Fe^{2+} and Fe^{3+} components. The sum of the two components is also shown, to compare with the experimental XAS.

3.6 Conclusion

In this chapter the synchrotron analysis of $LaTiO_3/LaFeO_3$ heterostructures was presented. Earlier works report the formation of a nonmagnetic band insulator at the isopolar interface between the $LaTiO_3$ and $LaFeO_3$. Based on the reports, there is charge transfer and a rearrangement of the Fe bands which can lead to a new nonmagnetic band insulating state at the mentioned interface.
Using the model described we were able to obtain the elemental depth concentration profiles of the entire heterostructure and describe it by the depth resolved susceptibility formula.
Based on the RXR fitting results of the $LaFeO_3/SrTiO_3$ heterostructure in various situations, we extrcted the fitting parameters determined the roughness and thickness of $LaAlO_3/LaFeO_3/LaAlO_3$ on $SrTiO_3$ substrate and it has proven to be useful for others as well. An unexpected 2D electron gas between interface of $LaAlO_3/SrTiO_3$ was detected which was not our goal but nevertheless an interesting aspect. Also using the result of the XAS analysis described we were able to successfully quantify the charge transfer to Fe using the spectral differences method and least squares fitting. our extracted Fe^{2+} spectrum can address the issue of the spin state of the charge transfer Fe state at the interface which is clearly a high spin Fe^{2+} spectrum. So we find that the predictions of the non-magnetic band insulating state at the interface were incorrect.

Overall this results represent a good first step on the path of understanding this system and shows promising vies toward fitting the RXR results of the other more advanced samples as a comprehensive project that can be tackled in the future.

4 XEOL Analysis of Oxygen Vacancies in Heterostructures

4.1 Introduction/motivation - 2D Electron Gases

In order to get to the topic of the role of oxygen vacancies in the heterostructures, I will first present a brief introduction of the relevant materials and the origin of the 2D electron gas. In particular, I will discuss the relevant oxide heterostructures, how 2D electron gases (2DEGs) are found to form at the interfaces, and I will present the two leading explanations for the origin of the 2DEGs. Lastly I will give an explanation of our objectives and method of research on these systems.

As mentioned in the previous chapters, oxide heterostructures have many interesting properties that have been focused on in recent studies. Correlated interactions in transition-metal oxides are the origin of many functional properties such as high temperature superconductivity, magneto-resistance and many others. The relatively recent discovery of a two dimensional electron gas at the interface of the insulating oxides $LaAlO_3$ and $SrTiO_3$ [55] was a peak point in studies of such properties and their application in all oxide structures and devices. Since the report from Ohtomo and Hwang was published in 2004,[55] this fascinating thin layer of 2DEG between two insulators has been the focus of many studies as it has properties such as a high electron mobility, superconductivity [20], a large magneto-resistance [56] and the fact that it can be seen on the length scale of few-nanometres [52].

A two-dimensional electron gas (2DEG), describes an electron gas with the freedom of moving in two dimensions but limited in the third. The electrons in this system are basically a 2-dimensional sheet buried in a 3D structure, and mostly in the interface between two oxide heterostructures [57]. Since the first discovery of this phenomenon, there has been debate over the origin of this 2DEG and there is yet much to study and understand about its nature in order to gain a prospect of the mechanism and to be able to tune its properties to a desired state. Further study can lead to

probable device applications which can be possible through increased tunability of these materials.

Using oxide heterostructures to discover and design functional properties has a vast platform of opportunities but the main and critical task here is to exactly understand how these structures react to various tuning parameters such as strain, polarity, layer thicknesses, and others. It is notable to mention that probing thin films with thicknesses in the nanoscale region is a complicated and difficult process and considering such thicknesses for a layer buried in an interface probing seems even more challenging.

There are two main hypotheses to explain the appearance of the 2DEG. Polar gating was the first mechanism that the conductivity at $LaAlO_3/SrTiO_3$ interfaces was explained with by the work of Ohtomo and his group [55]. This theory begins with the observation that the $LaAlO_3$ (001) surface is polar. This means the individual LaO and AlO_2 layers are charged (with +1 e and -1 e per unit cell, respectively, where e is the elementary charge). On the other hand, the (001) surface of $SrTiO_3$ is not polar, since the SrO and TiO_2 layers are charge neutral. As shown in Figure 4.1, when $LaAlO_3$ is grown on $SrTiO_3$, the alternating charge density in each layer leads to a non-cancelling electric field. The integration this electric field leads to an electrostatic potential which continues to grow as each new layer is formed. As an insulator, in $LaAlO_3$ the valance band has an energy below the Fermi level but when grown thicker than three unit cells, the growing potential means that its energy will rise above the Fermi level allowing electrons from the valence band near the surface to move to lower energy states in the conduction band of $SrTiO_3$ at the interface. After significant research efforts, there are many strong and weak points about this theory and still there is much to be done in this area.

Another hypothesis which will be the focus of this chapter and the work, is the role of oxygen vacancies in supplying the free electrons to form the 2DEG and make the conductivity possible. As illustrated in Figure 4.2, one particular method for synthesizing such a 2DEG is through low temperature film growth, which can lead to the formation of oxygen vacancies located at the interface, donating the charge for the 2DEG formation [56, 17]. Oxygen vacancies are known to introduce a shallow intragap donor level close to the conduction band of STO, and their action may be specific to this one substrate.

For further discussion about the two hypothesis mentioned, it is helpful to look into structural aspects of the interface. It is certain that physical structure of a system plays an important role

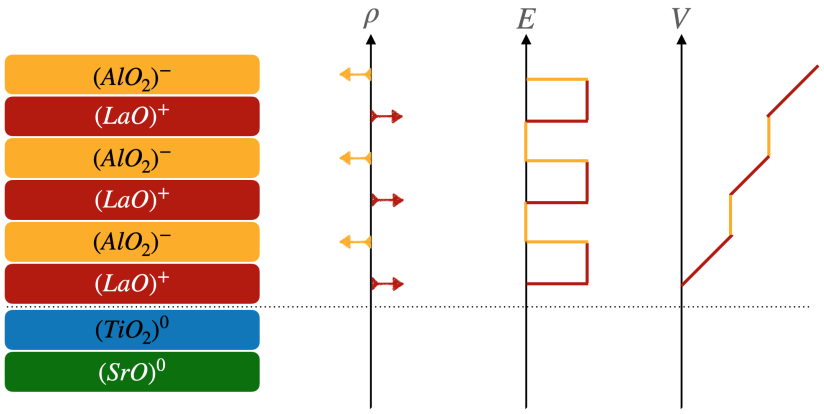

Figure 4.1: In polar LAO, after the potential builds up by increasing the layers demonstrates the electronic polar catastrophe. ρ is charge density, E is electric field and V is potential. Image reproduced from [17].

in the emergent properties of an interface but based on the evidence from recent experiments on the conducting oxide interfaces, chemical reactions can have an important role and should be investigated further. Chemical interactions in these kind of systems can be categorized into different groups. One of which is the redox, thought to be a main reason for the conductivity and appearance of the 2DEG between LAO/STO interface. Although as mentioned before, there is still ongoing debate on the origin of this 2DEG.

Emergent properties in an STO substrate, with focus on the oxidation of the top layer and reduction of the STO surface, are strongly correlated to the substrate's temperature and the background oxygen pressure during the growth of the film [17]. For this reason it is expected to see sensitivity to electrochemical reaction situations and limits in thermodynamical and kinetic aspects which makes studying this material even more complex. To further understand the properties of this interface one can look into the reasons that makes STO a perfect substrate for the interfaces that have such interesting properties embedded in them. The lattice structure of STO can be matched with other provskite oxide structures and result in an epitaxial heterostructure. Also this material has a strong electronic correlation which is responsible for many of the emergent properties seen by experiments during recent years. In order to discuss the origin of the 2DEG at the LAO/STO interface, it is also worthwhile to look into the properties of the oxides themselves. The theory of a pure electronic reconstruction is now modified into a much more precise theory that this built in potential is compensated by the positively charged surface which takes us to the theory that

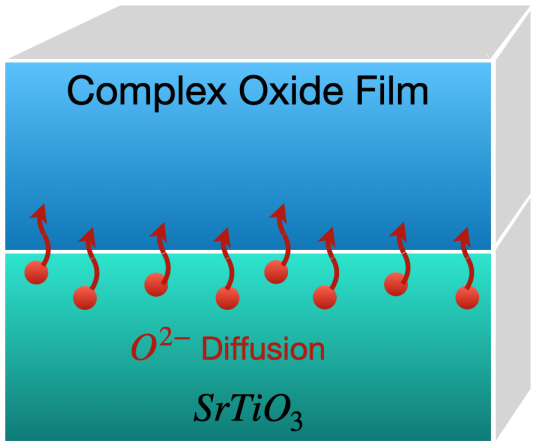

Figure 4.2: A schematic to show redox reaction at the interface of STO based interfaces. Image reproduced from [58].

oxygen vacancies can act as charge donors and be responsible for the emergence of the interesting 2DEG layer. Experimentally this theory is also difficult to explore since for that purpose we need to consider the redox reactions of the STO surface upon deposition of the oxygen deficient LAO. Figure 4.2 demonstrates the redox reactions which can lead to the removal of oxygen from the STO near the interface during film growth.

There is much research in this area studying the effects of different factors that have impact on the appearance and using the properties of the 2d electron gas. Different methods of spectroscopy has been applied to probe this thin layer, such as resonant soft x-ray reflectometry and diffraction, photo-luminescence spectroscopy and many others. Despite the vast research in this subject very little is known about the confinement of the oxygen vacancies to the interface or their detailed depth distribution into the substrate.

Our study focuses on the role of oxygen vacancies in the buried layer of 2DEGs and the oxygen vacancy type systems and we aim to find a way to directly isolate and see the presence of oxygen vacancies at the interfaces that follow the same structural pattern. The importance of this task does not limit to figuring out the origin and the verifying that oxygen vacancies are truly responsible for the understudy mechanism, but also leads to the important understanding of the elusive subjects such as the confinement of these vacancies to the interface, how we can engineer methods to control them and use the results to not only clarify the debates but also step towards functional device

fabrication.

Recent studies [59, 60, 61] show that at lower growth temperatures there have been reports of a noticeable increase in mobility of STO based 2DEGs which can provide a good example to show the promising improvements of this class of studies. By studying different samples and arranging the interface components in different ways we hope to extract a depth profile of the oxygen vacancies at the interface. One method is to use other compatible provskite oxide such as epitaxial, crystalline Al_2O_3 grown at high temperature, and disordered $LaAlO_3$ grown at low temperature or to have different thicknesses of the capping.

For most of STO heterostructures there is a high carrier density in the 2DEGs. The electrons that are at or near the interface have a lower mobility in comparison to the electrons that account for only a small fraction of the 2DEG population and are further away from the interface. Originally the method for enhancing the electron mobility is by introducing a layer which separates the electron gas from the donor charges, however in the STO heterostructures the mentioned condition of low and high mobility carriers simultaneously, make this conventional method not a suitable path to take. For the experimental part of our research we use energy dependant XEOL (discussed in chapter 2 section 5). It is known that oxygen vacancies in $SrTiO_3$-substrates provide strong photo-luminescence. This can be used as a method to detect vacancies which is the reason that makes XEOL an excellent tool to study and probe this delicate and complicated phenomena. Our research focuses on two samples, Al_2O_3 and $LaAlO_3$ on a $SrTiO_3$-substrate to study with XEOL in order to determine their vacancy depth profiles. Based on earlier works, for the Al_2O_3 sample we expect to have vacancies throughout the sample and studies on the interface between $LaAlO_3/SrTiO_3$ shows vacancies localized near the interface. These different vacancy depth profiles we can provide a good test case for the method.

4.2 Theoretical Motivation

For the theoretical part of our research we began by considering the attenuation length of the materials involved in our samples and the fact that each material has a unique energy dependent attenuation coefficient. The effect of this attenuation is quantified by the Beer-Lambert law which

relates the attenuation of light to the properties of the material through which the light is travelling,

$$I(E, z) = I_0 e^{-\mu(E)z}, \tag{4.1}$$

where $I(E, z)$ is the intensity of the beam at the penetration depth z and is a measure of the exponential decay of a beam of photons of initial intensity I_0 at energy E through a sample. The attenuation length μ is defined as the penetration depth where the light(x-ray) intensity will decrease by the factor of $1/e$ from its initial incident intensity value. This means that a 1-1/e portion of the x-rays is absorbed within an attenuation length.

Lambert's law states that the loss of light intensity when it propagates in a medium is directly proportional to intensity and path length. This law is commonly applied to chemical analysis measurements and is used in understanding attenuation in physical optics, for photons and neutrons. Via the relations mentioned we can calculate the fraction of x-rays transmitted through the material as a function of depth, which then can result in a fraction of x-rays absorbed in each assumed layer by subtracting the initial intensity of the incoming x-ray beam.

As introduced in Chapter 2, the x-rays incident upon the sample can lead to x-ray excited optical luminescence via various complex mechanisms. Liu et al showed that oxygen vacancies in $SrTiO_3$ do lead to strong luminescence in the 350-500 nm range [62]. Their result presents a comparison of amorphous and crystalline LAO/STO heterostructures based on electrical and optical measurements. Based on the the photoluminecense spectra of the amorphous LAO/STO heterostructure, the intensity increases with decreasing oxygen partial pressure which they attributed to the creation of oxygen vacancies in the STO substrates near their interface during deposition.

Based on this observation of oxygen vacancy luminescence, our x-rays being absorbed should lead to XEOL if they happen to be absorbed at or near an oxygen vacancy site. This renders XEOL a great path to map the depth dependence of the oxygen vacancies. To accomplish this mapping, we must quantify the depth dependent absorption of x-rays, as done in the following.

We consider depth dependent slices of uniform thickness t in our material, and for a given energy use symbol A to denote the fraction transmitted through the layer. If the initial intensity of x-rays incident upon the first slice (i.e. the surface) is I_0, then the amount absorbed in the first slice is

$(1-A)I_0$. So the light intensity incident on the second layer is AI_0 and $A(1-A)I_0$ will be absorbed on the second layer, leaving the amount transmitted through the second layer to be $(1-A)^2 I$. For n layers, the fraction of the initial intensity absorbed in the ith layer, A_i, will be

$$A_i = A\left(1-A\right)^{i-1} \tag{4.2}$$

Going back to Beer Lambert law, we can therefore compute the fraction of x-rays absorbed in a slice of thickness dz at depth z from

$$I_{abs}\left(E,z\right) = I\left(E,z\right) - I\left(E,z+dz\right) = I_0 e^{-\mu(E)z}\left(1-e^{-\mu(E)dz}\right) \tag{4.3}$$

The theory above tells us what fraction of x-rays are absorbed in each slice throughout the depth of our sample. In each of these slices there will be some concentration of oxygen vacancies, and the XEOL produced will be a product of the fraction of x-rays absorbed and the concentration of vacancies in the region,

$$I_{xeol}\left(E,z\right) = f\left(z\right) I_{abs}\left(E,z\right) \tag{4.4}$$

where $f\left(z\right)$ is the concentration of oxygen vacancies in the slice.

The total XEOL intensity is then the integral of this expression over the entire thickness of the sample,

$$I_{xeol}\left(E,z\right) = \int f\left(z\right) I_{abs}\left(E,z\right)\, dz \tag{4.5}$$

Since a single incident photon energy leads to only a single measured XEOL intensity, it is not sufficient to determine the vacancy profile. However, if measurements are made at many different incident energies, for which the distribution of absorbed energies is different due to different attenuation lengths, then the profile of vacancies can be determined.

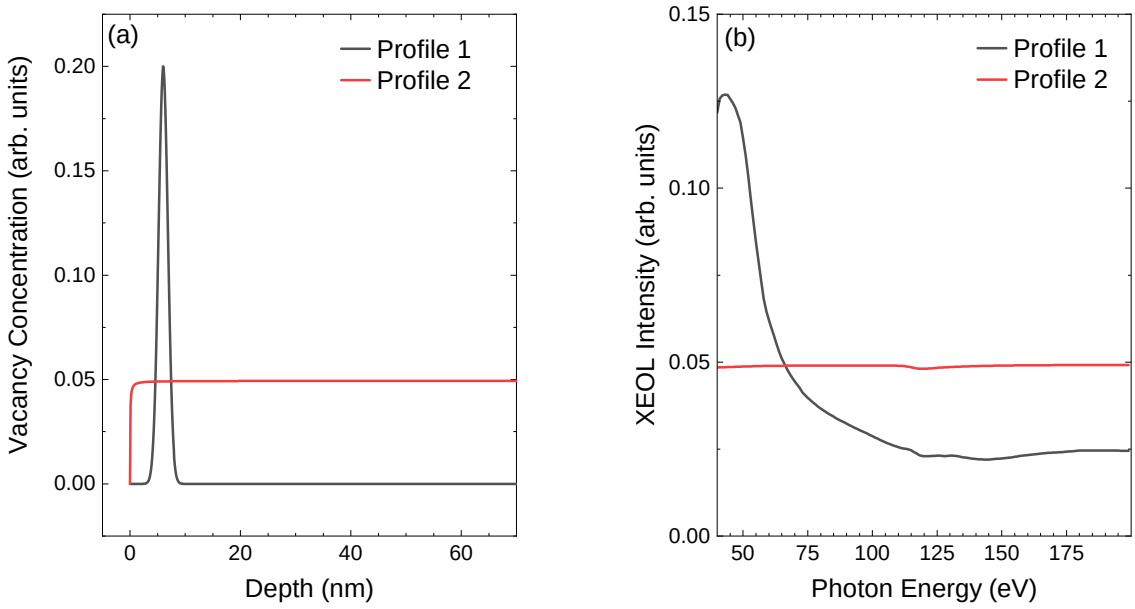

Figure 4.3: Figure (a) shows two vacancy concentration profiles for an LAO on STO example as a function of depth. (b) shows how these two profiles lead to two different XEOL energy dependences.

As an example, see Figure 4.3 where we simulate two extreme cases of vacancies located at the interface of LAO/STO or spread homogeneously throughout the bulk of the STO. It is evident the energy dependence of the XEOL is quite different in each case, which exhibits the sensitivity of the technique to the profile shape. For the case where vacancies are located near the surface, one sees that the XEOL intensity gradually decreases for higher energies. This is because the x-rays probe deeper at higher energies, and therefore fewer are absorbed in the region of oxygen vacancies at the surface. In contrast, when oxygen vacancies are spread deeper into the bulk, the XEOL intensity grows at higher energies, as fewer x-rays are absorbed near the surface where there are few vacancies.

In practice, we assume a particular parametrized profile shape, and fit the resulting simulated XEOL energy dependence to experiment by varying the parameters of the profile. The true type of profile shape is not known to us, so we consider a range of possibilities. Our profile shapes are given below, where in each case there are three fitted parameters, including a simple scale factor C, a central or starting depth z_0, and a width parameter w. Note that in practice we have rounded

the corners of the rectangular profile to improve the convergence properties of the fitting algorithm. The definitions of our profile shapes are:

$$\text{Exponential decay}: \qquad f(z) = \begin{cases} Ce^{-(z-z_0)/w}, & z \geq z_0 \\ 0, & z < z_0 \end{cases} \tag{4.6}$$

$$\text{Gaussian}: \qquad f(z) = Ce^{-(z-z_0)^2\left(4\ln 2/w^2\right)} \tag{4.7}$$

$$\text{Rectangular}: \qquad f(z) = \begin{cases} C, & |z-z_0| \leq w/2 \\ 0, & |z-z_0| > w/2 \end{cases} \tag{4.8}$$

$$\text{Step 1}: \qquad f(z) = C\left(\arctan\left[(z-z_0)/w\right] + \frac{\pi}{2}\right) \tag{4.9}$$

$$\text{Step 2}: \qquad f(z) = C\left(\arctan\left[(z_0-z)/w\right] + \frac{\pi}{2}\right) \tag{4.10}$$

For a given data set we try all profiles and report the one that provides the best fit and is therefore the closest approximation to the true profile. After an introduction to the experimental procedures in the next section, we show the results of our fitting in the following section.

4.3 Experimental Details

In this section I will give a brief description of the beamline we used to gather data and its relative properties along with the devices that are used in this branch, and how they affect the data acquisition. Then a detailed explanation of the method we applied for the data acquisition process will be discussed.

XEOL measurements on our samples were performed at the Variable Line Spacing Plane Grating Monochromator (VLS-PGM) beamline at the Canadian Light Source. Facilitating research in materials of both fundamental and applied nature, the VLS-PGM beamline provides high resolu-

tion, low energy spectroscopic studies. Based on the requirements and performance expectancy, the beam line has an optical design that is also implemented at several radiation centers over the years. The construction of the VLS-PGM beamline started in 2004, among the first beamlines of the CLS. The photon source has a permanent magnet insertion device (with 185 mm period length) in a straight section which is shared with another soft x-ray beamline. The design of this beamline consists of three variable line spacing plane gratings: low energy grating (LEG): 5 – 38 eV; medium energy grating (MEG): 25 – 120 eV; and high energy grating (HEG): 90 – 250 eV which all together are designed to cover the desired energy range thoroughly. As this beamline was designed with the purpose of having a highest resolution while covering the energy range of 5-250 eV, there is an entrance slit placed in the beam line end station and also a monochrometer based on a spherical focusing mirror to have low contributions that are caused by higher orders. This design brings advantages such as energy can simply be scanned by a grating rotation and optimum resolution that made minimizing the grating aberrations possible via variable spacing parameters.[63]

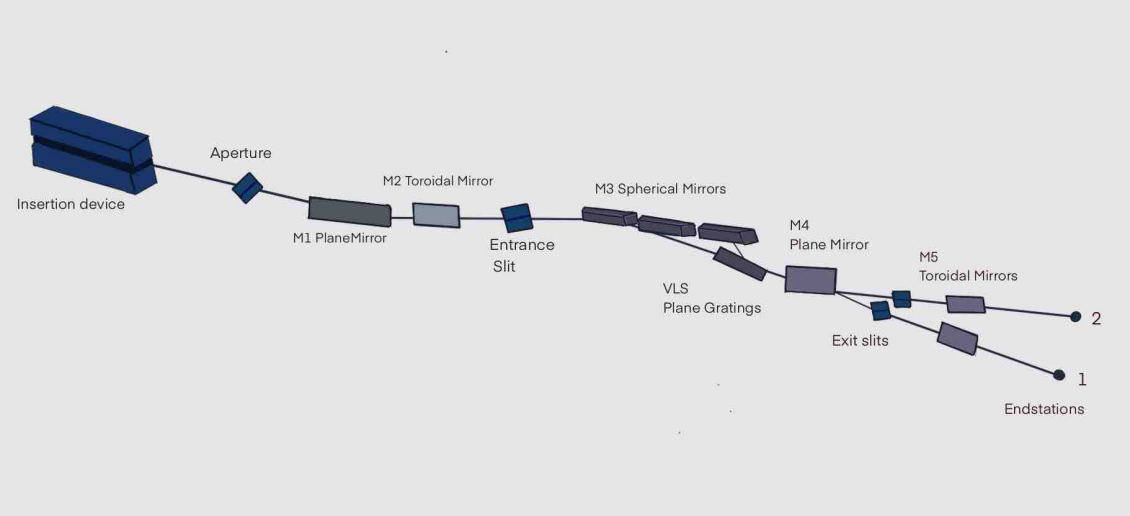

Figure 4.4: A schematic of the beamline and its components from the insertion device to the endstations. Figure reproduced from [64].

Figure 4.4 shows a schematic of the beamline and its components. The first optical component is a C-coated plane mirror which is used to deflect the photon beam horizontally by three degrees to have a branch by the SGM beamline that shares a magnet. It is also expected that this mirror absorb the unwanted power up to 450 W. Also, it is notable to mention that the effect of tangential figure errors caused by this mirror which is in the horizontal direction is much smaller then the

horizontal spot size.[64]

The second mirror which is also C-coated has an optical function of deflecting the beam by 9 degrees horizontally. The main purpose of this mirror is aligning the beam horizontally and demagnifying the source vertically onto the entrance slit. After the second mirror, there are three spherical mirrors, they were chosen specifically to decrease any decay to the resolution that might have been caused by the optics in between the entrance and exit slits. These three spherical mirrors are each fixed at a certain angle in such manner that their focusing does not differ significantly from mirror to mirror in order to keep a good overall horizontal focusing. Consequently, the zero order angles on the gratings are chosen similar to the spherical mirrors for the same reason. The monochromator which plays an important role here, uses three variable line spacing gratings to properly cover the energy range between 5 and 250 eV. Passing through these mirrors and gratings and their specific angles of grazing incidence and the gratings zero order angles, the third or higher order contributions are notably suppressed.[63]

Before the exit slit a plane mirror is inserted to guide the photon beam and supply the other exit slit that belongs to the other end station. To complete the focus of the beam spot to optimum size, after each slit there are toroidal mirrors inserted into both of the experimental situations.

Using a toroidal mirror, the beam is focused through an entrance slit and is deflected horizontally and since by using the quadratic variation in the line spacing of each grating the deviation is zeroed, one can have a good energy resolution. The mentioned spherical mirrors deflect beam in the dispersion plane and are fixed each at a grazing angle, thus the energy is simply scanned with a grating rotation. This beamline is divided into two branches and each have a pumped chamber housing an I_0 mesh, a Si photodiode (sensitive to visible light) and necessary filters.[64]

This beamline has an expected delivery of 9×10^{11} photons/s per 100 mA and the photon fluxes are regularly measured and has been normalized, as seen in Figure 4.5, to 100 mA of the ring current and to 50 μm slit settings. The features at 100 and 50 eV are due to the first and second order contributions, respectively.

For the XEOL measurements, the sample were measured at a nominal angle of 19 degrees, which corresponds to an angle of 45 degrees between the sample surface and incident radiation. Our samples were excited at an energy range between 30 and 230 eV and the luminescence spectra were collected by at optical spectrometer which was 45 degrees to the sample surface and at a

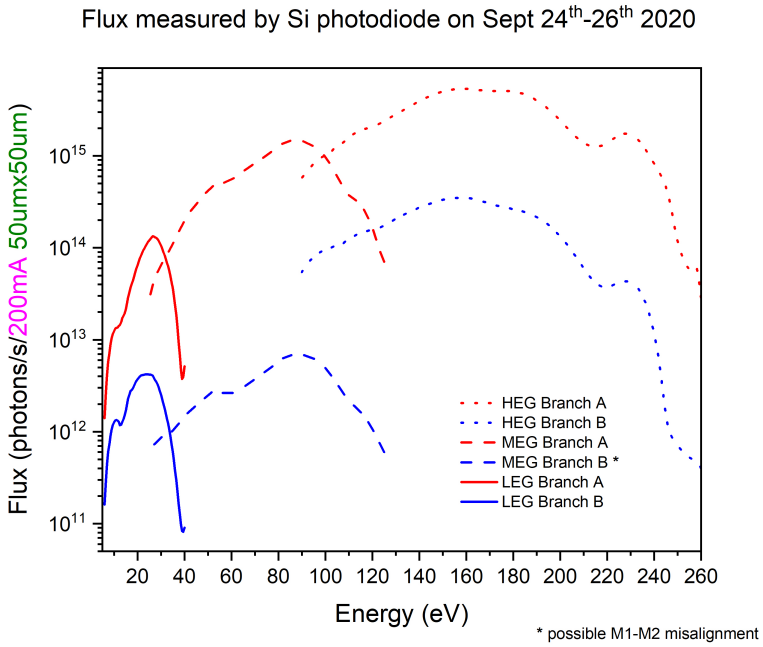

Figure 4.5: The most recent fluxes measured for both branches of the VLS-PGM beamline. Image from the beamline website [26].

right angle to the incident radiation. Because we want to perform a quantitative analysis, accurate normalization of the beam intensity is necessary over all energies of the experiment. Typical gold meshes used for I_0 measurements do not provide this, as their responsivity changes with energy in a way that is difficult to quantify. Instead, the Si photodiode at the beamline was utilized for normalization. During each beamtime, measurements with the beam directly hitting the photodiode were performed, and were normalized to the ring current. This signal was then also normalized by the responsivity of the photodiode, using data sheets provided by the manufacturer. When measuring the XEOL, we then divide by the ring current, and then our reference I_0 determined using the photodiode procedure.

For our measurements, we planned to use two experimental control parameters to probe the depth distribution of the vacancies - the incident photon energy (thus varying the attenuation length) and the incident angle of the photons on the film surfaces. The first step after introducing samples to the chamber was to check the linearity of the XEOL signal on the incident photon flux. To do this, we detuned the undulator to record the XEOL intensity as a function of the changing photon flux, since its important to have a linear behaviour. This process was repeated for each sample and each change of gratings that we measured.

After verifying linearity, we set the incident angle to 45 degrees, and collect XEOL spectra as a function of incident photon energy. This first involves a coarser stepping of photon energies (5 eV or in some cases due to shortage of time, 20 eV steps) over the PGM energy range, where the absorption cross section of the film varies. Next step was to collect a more detailed PLY XEOL maps at the Al(L23), Zr(M45), and La(N45) edges. These edges further strongly vary the attenuation length of the photons in the film, and thus change the probing depth for oxygen vacancies. Next step was varying the probing depth via the incident angle of photons on the sample surface, which we were not able to apply in practice due to the situation of the beamline and calibration. Based on the results this control parameter could be a suitable next step for future research.

4.3.1 Growth

In this section a short description of our samples growth condition which was performed by the collaborators is presented. The heterostructures were grown on TiO_2-terminated STO substrates by using pulsed laser deposition (PLD) in an oxygen atmosphere of $\sim 10^{-4}$ mbar. In the PLD process, a high power pulsed laser is focused on the target material in a vacuum chamber. The atoms of the target material are then ablated and settle on a substrate target, allowing layer by layer growth of the thin film. By using a KrF laser with a 1Hz repetition rate and 1.5 J.cm^{-2} laser fluence during the ablation process. For the growth process the target-substrate distance was fixed at 5.6 cm. For the disordered LAO sample the film deposition was done at room temperature (300K) by using a single crystalline LAO target. The film growth process was monitored by in-situ high pressure reflection high-energy electron diffraction (RHEED) for both of the samples. Similarly the Al_2O_3 thin films were grown by PLD with the same laser fluence and repetition. As targets, commercial Al_2O_3 single crystals were used. During deposition, the oxygen pressure was fixed at $\sim 10^{-4}$ mbar with a deposition temperature of 600 °C. After film deposition, the samples were cooled down to room temperature at the deposition pressure.

4.3.2 Determination of Film Thicknesses

In order to analyze the experimental XEOL data using the theory described earlier, the thickness of samples need to be determined. To do so, RXR measurements were performed at the REIXS beam line of the CLS.

For both samples the incident energy of the x-rays was 501 eV, to get the optimum interface fringes. The experimental data of the reflectometry was fitted in a simple least squares fitting method similar to the fitting process mentioned in the previous chapter. The reflectivity fitting program ReMagX was used for these simple fits. Figure 4.6 shows the result of the fitting model compared to the experimental reflected intensity as a function of momentum transfer for LAO/STO, while Figure 4.7 shows the result of fitting model to the experimental data of Al_2O_3/STO as a function of momentum transfer. The result of successfully fitting the model to our experimental RXR data gives the thickness of each sample which is a necessary part of our XEOL data analysis process.

It is notable that for the fitting process here, as its common in RXR fitting, one has to take into account the sensitivity to surface contamination that most samples have after exposure to the atmosphere. Thus in the fitting process a small amount of carbon surface contamination is included. In the end, our fitted thickness for the LAO film is 4.62 nm and the fitted thickness of the Al_2O_3 film is 4.36 nm.

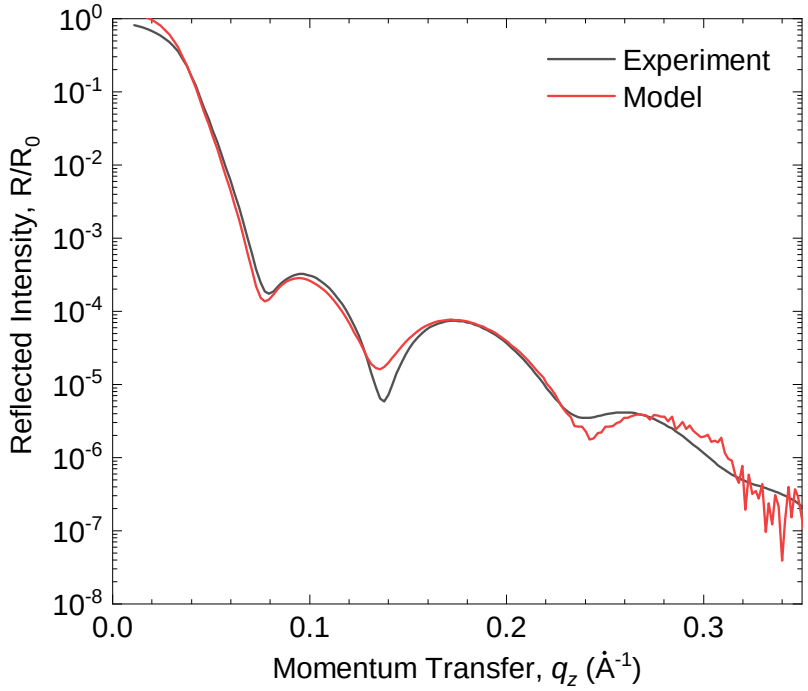

Figure 4.6: Experimental and fitted resonant x-ray reflectivity curve for the LAO/STO sample.

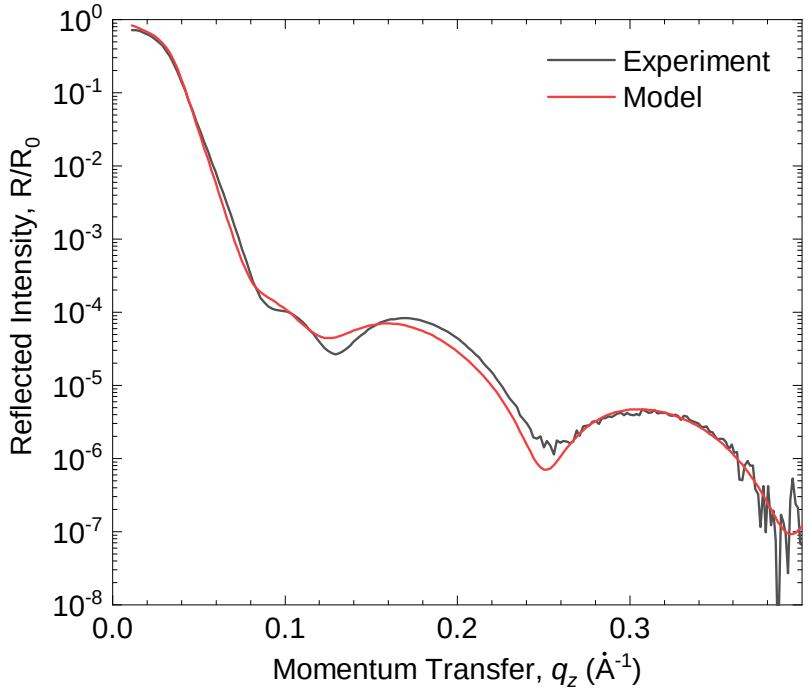

Figure 4.7: Experimental and fitted resonant x-ray reflectivity curve for the Al_2O_3/STO sample.

4.4 Fitting Results

In this section the XEOL analysis results of our two samples are presented. After introducing the results of the fitting and the luminescence profile that lead to it, there will be a discussion of the important findings and their meaning in regard to the study and finally the importance of our research based on our results will be discussed. The raw data is normalized by I_0 (the intensity of the incoming beam) and the photo diode measurements to ensure linearity and minimal noise. Various profile shapes were tried out to find the one that matches the luminescence spectra of each sample in a specific wavelength region.

4.4.1 Results of Al_2O_3/STO Sample

In Figure 4.8, the luminescence spectra recorded by the XEOL detector is presented. In order to improve the statistics for displaying the peaks, the multiple luminescence spectra taken at various incident energies are summed together. Based on the features in the normalized XEOL spectra as a function of wavelength, the results are divided into high wavelength region (for this sample from

350 to 700 nm) and low wavelength region (from 700 to 1000 nm). Since the reason for having two wavelength regions is not specifically clear, we analyse them separately with our depth profiling procedure in order to gain better insight.

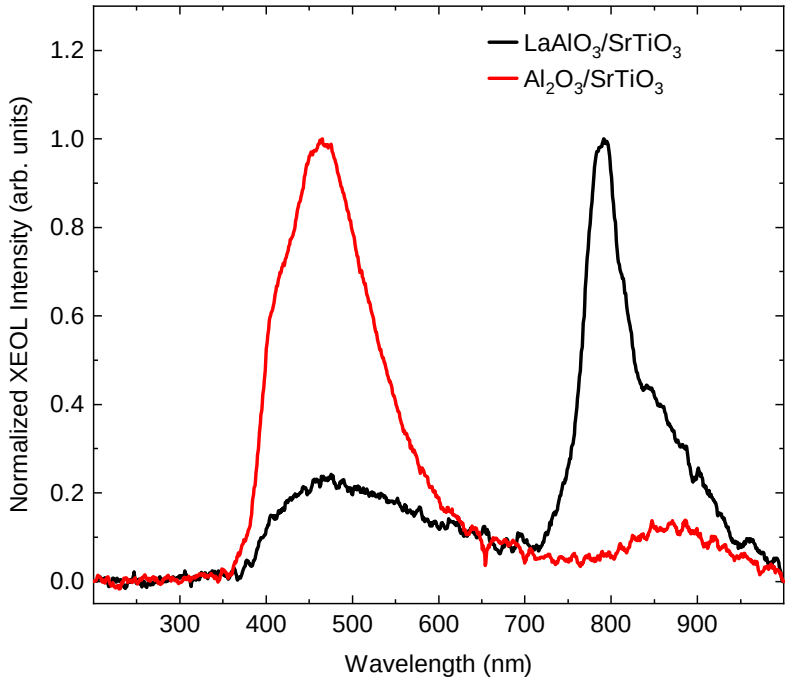

Figure 4.8: Normalized XEOL spectra, summed over various incident energies, as a function of wavelength.

For this sample, in the low wavelength region, Figure 4.9 shows the XEOL spectrum as a function of energy with the range up to 200 eV. As one can see in the Figure, there is a feature showing higher optical luminescence at about 70 eV and using our fitting function and assumed oxygen vacancy profiles we were able to get a reasonably good fit to the experimental data.

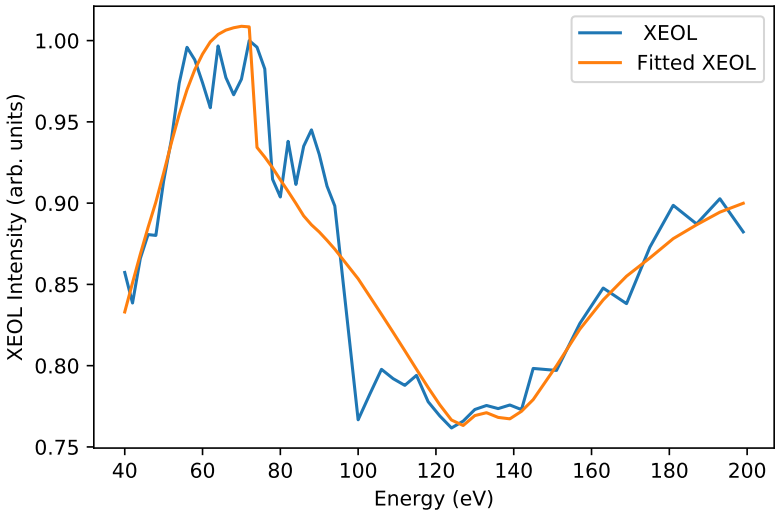

Figure 4.9: Comparing experimental and fitted XEOL for Al_2O_3/STO Sample in low wavelength region.

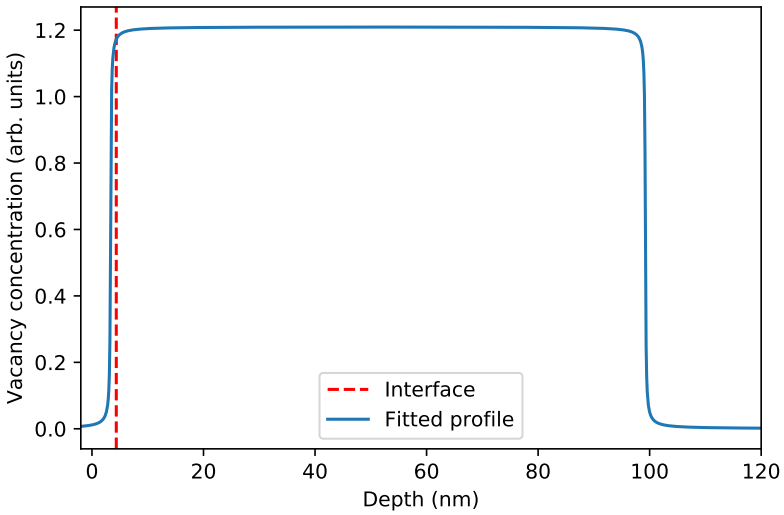

Figure 4.10: Luminescence profile fitting result for Al_2O_3/STO Sample in low wavelength region.

Figure 4.10 shows the luminescence profile fitting result of Al_2O_3 grown on top of a substrate STO in low wavelength region. This crystalline film was grown at high temperatures and this growth conditions play an important role in the formation of the vacancies. As it is shown in Figure 4.10, as a function of depth there is a component that gives a profile which spreads about 100 nm into

the bulk. This profile fitting had the best result using a rectangular function as the assumed profile to have the closest fitted XEOL to the experimental data.

In Figure 4.11, the comparison of the experimental and fitted XEOL in the high wavelength region is presented. As there is no decrease in intensity at higher energies, we expect a vacancy profile which spreads deeper into the bulk. As shown in the Figure, we are able to achieve a good fit to the experiment using our model.

In the high wavelength region the mentioned component gives a luminescence profile that extends very deep into the substrate as shown in Figure 4.12 and it is homogeneously spread through the bulk. We used a step function as an assumed profile to get the optimum results here. This important finding is in well agreement of what was expected for this sample. Given the high temperature growth condition the presence of oxygen vacancies is not expected near the interface but rather diffused into the bulk. As discussed above, there are two different depth distributions present in the analysis of this sample. One can be the result of the vacancies leading to the rectangular growth profile coming from the growth process and perhaps the distribution in the high wavelength region is due to a type of impurities that are evenly spread out through the STO substrate even before the growth procedure.

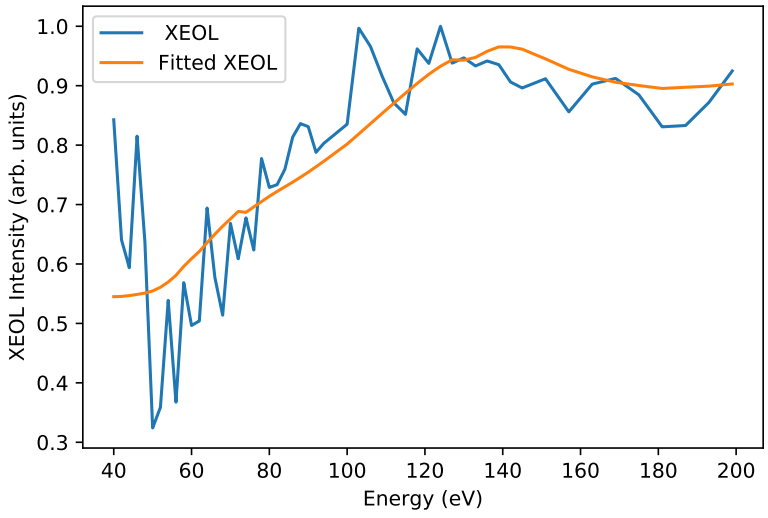

Figure 4.11: Comparing experimental and fitted XEOL for Al_2O_3/STO Sample in high wavelength region.

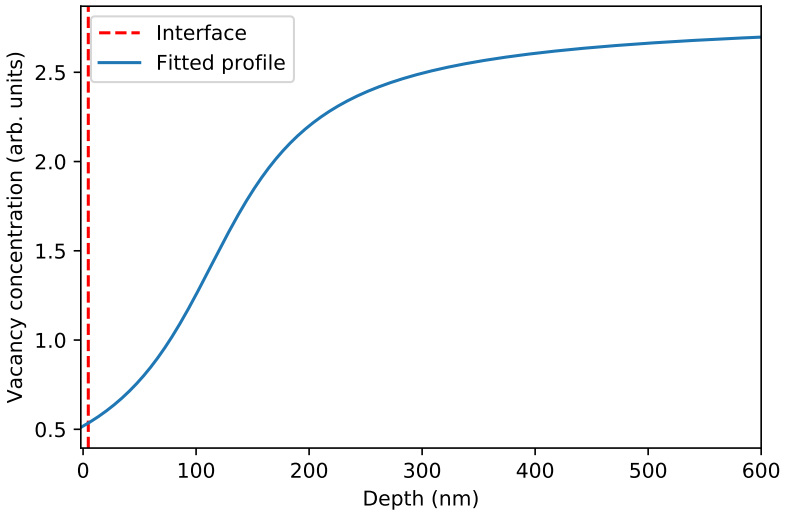

Figure 4.12: Luminescence profile fitting result for Al_2O_3/STO Sample in high wavelength region.

4.4.2 Results of $LaAlO_3$/STO Sample

For the $LaAlO_3$/STO sample, the wavelength region is also divided into low (from 350 to 600 nm) and high (from 725 to 1000 nm) regions, as shown in Figure 4.8. Comparing the experimental and fitted XEOL in Figure 4.13 in low wavelength region, there is a sharp feature at around 120 eV and when fitted is in good agreement with the experimental data. From this Figure one can gather that the sharp peak at about 120 eV is due to the resonance edge of lanthanum corresponding to the excitation from 4d to 4f. This important fact, points out that the XEOL is coming from the film.

As shown in Figure 4.14, the component in the low wavelength region leads to a luminescence profile that is localized at the very surface of the film. This might be due to defects or vacancies at the LAO surface. The profile shape which gave the best fit for this analysis was the exponential decay function.

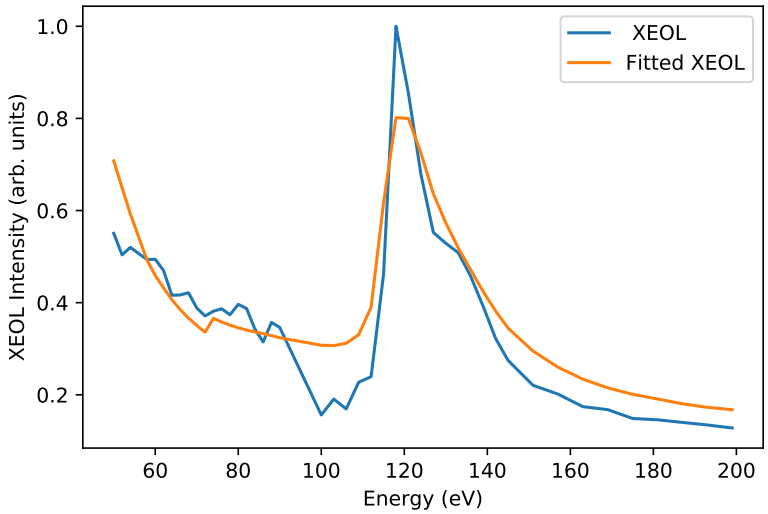

Figure 4.13: Comparing experimental and fitted XEOL for $LaAlO_3$/STO sample in low wavelength region.

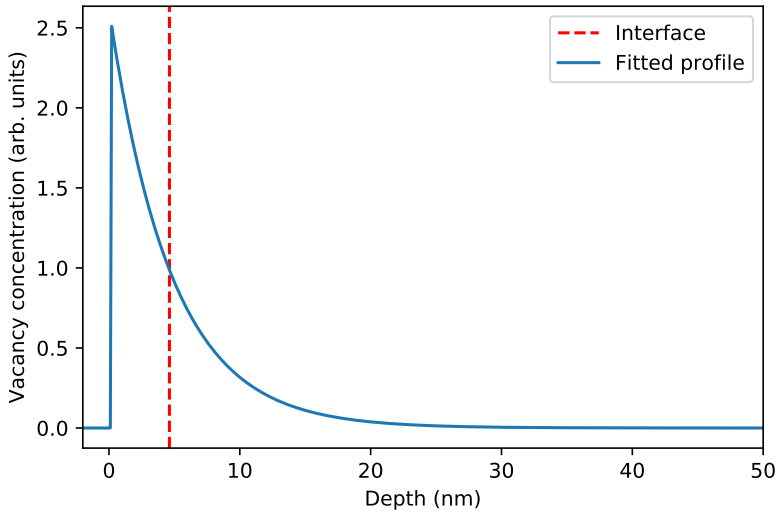

Figure 4.14: Luminescence profile fitting result for $LaAlO_3$/STO sample in low wavelength region.

In high wavelength region the comparison of the experimental and fitted XEOL is presented in Figure 4.15. Here the luminescence spectra as a function of energy is decreasing from its maximum until 120 eV which gradually stabilizes and remains roughly constant until 200 eV. Generally with an increase in the energy level, the detected XEOL will decrease if the luminescence is coming

from elements near the surface and the XEOL will increase if they are deep into the substrate. In Figure 4.16 the luminescence profile of the component in the high wavelength region is presented. A Gaussian profile gave the best results while fitting for this profile. The luminescence profile shows that the vacancies are localized near the interface.

This very interesting result shows consistency with what we had expected and the vacancies that stay localized near the interface, form the 2DEG. As mentioned above, this localization of the vacancies formed by redox reactions near the interface, is likely due to the low growth temperature.

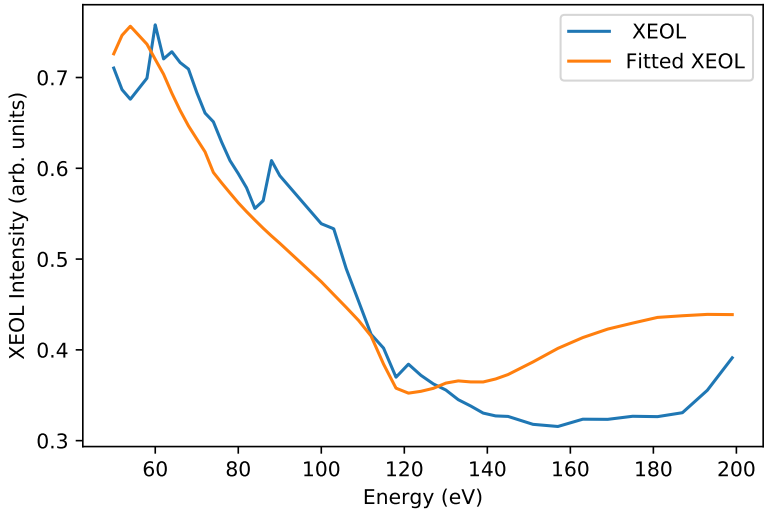

Figure 4.15: Comparing experimental and fitted XEOL for $LaAlO_3$/STO Sample in high wavelength region.

As mentioned previously, the work of Z. Q. Liu *et al* [62], shows luminescence spectra of LAO/STO and indicates that oxygen vacancies give luminescence signals around 400 nm. With our approach too we see luminescence at higher wavelengths as well. It should be mentioned that currently we cannot prove that the luminescence observed in our results are due to oxygen vacancies, however by consulting the mentioned paper and our promising results being consistent with our expectations, there is a strong argument that these defects which are providing the luminescence can in fact be caused by the oxygen vacancies. Comparing the results from this two different samples results in useful gatherings such as the importance of growth condition and how if the sample is grown in high temperatures the vacancies will be homogeneously spread through the bulk, how changes in the optical luminescence spectra can indicate the position and localization of the

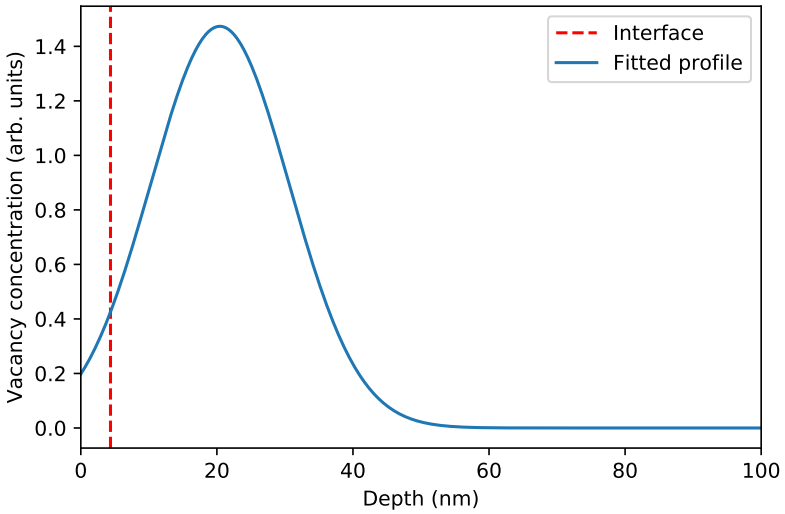

Figure 4.16: Luminescence profile fitting result for $LaAlO_3$/STO Sample in high wavelength region.

vacancies abruptly.

Overall using XEOL as a new approach for studying defects and mapping the position of the oxygen vacancies renders useful road-map and is proven to have the potential for further research. It is notable that the $Al_2O_3/SrTiO_3$ sample can be a great example of non interface vacancies and can be used as a reference while analyzing the other samples luminescence spectra.

4.5 Conclusion

In this chapter the XEOL analysis of oxygen vacancies in heterostructures was discussed. Our main goal was to study the role of oxygen vacancies in the 2DEG formed at the interface of LAO/STO heterostructures and to extract a depth profile of the oxygen vacancies using the never used XEOL for this purpose. In the PGM beamline of CLS, we gathered our experimental PLY XEOL measurements at edges of the key elements, thus varying the probing depth. Then we analysed the experimental data using a curve fitting function and in our script that is able to create a theoretical XEOL by having an assumed luminescence profile. For the $Al_2O_3/SrTiO_3$ sample our fitted luminescence profile showed a vacancy profile that spreads about a 100 nm into the bulk in low wavelength region and a profile which spreads homogeneously into the bulk in high wavelength region.

And for the LAO/STO sample, the results of successfully fitting the theoretical XEOL to the experimental data concluded to a luminescence profile that was localized at the very surface of the film in low wavelength region which might be due to defects or vacancies at the surface of the LAO layer. In the high wavelength region, the results lead to a luminescence profile that shows the vacancies in the STO substrate are localized near the interface. Based on the results satisfying the expectations and consulting with previous works, we concluded that the luminescence observed in our data there is a strong argument that they are the oxygen vacancies responsible for the appearance of the 2DEG. Overall, our successful results prove XEOL to be an innovative method ideal for studying defects and oxygen vacancies in oxide heterostructures and can be used as a new method with great potential for further research.

5 Conclusion and Future Work

As the basis of devices and modern society is strongly correlated with material science, any advances in this field would affect technology in many aspects. To study the relative performance of materials in a given application, the main step is determination of structure properties correlation. Many recent advances focus on complex oxide heterostructures and their interfaces due to their interesting electric and magnetic properties and the possibility of being tuned to a desired stage.

Transition metals in the d-block of the periodic table with a partially filled d sub shell and transition metal oxides are the foundation of our complex interfaces with their interesting properties such as magnetism, charge transfer transitions and superconductivity to name a few. These building blocks can be put together as heterostructures and thin films which host many interesting phenomenons such as the 2DEG at their interface are bedding to a complex field of research.

One of the projects discussed here was the RXR analysis of oxide heterostructures involving layers of the anti-ferromagnetic Mott-Hubbard insulator $LaTiO_3$ and layers of the anti-ferromagnetic charge transfer insulator $LaFeO_3$ based on existing data. Using a combination of XAS and RXR on several samples, the main goal was to quantify charge transfer at the interface and determine subsequent changes in magnetic properties driven by this charge transfer.

X-ray absoprtion spectra (XAS) and resonant x-ray reflectometry (RXR) data were analyzed to study the charge transfer and magnetic properties. Elemental depth concentrations were obtained from a detailed quantitative fitting of the RXR data using the program QUAD. Using this model, we have so far determined the roughness and thickness of $LaAlO_3/LaFeO_3/LaAlO_3$ on $SrTiO_3$ substrate and it has proven to be useful for others as well. An unexpected 2D electron gas between interface of $LaAlO_3/SrTiO_3$ was detected and quantified which was not our goal but nevertheless an interesting aspect. Our XAS analysis qualitatively showed a consistent level of charge transfer for the sample containing LTO and we detected no charge transfer to Fe for the LAO sample. Also based on our results, the spin state of the charge transfer Fe was different from the predictions of

earlier theory work and was found to be a high spin state. the observed high spin state indicates that the Hund's rule stabilization was greater than the crystal field splitting and breaking of degeneracies of electron orbital states to different energies was not the case here.

The main project which was discussed in chapter 4 is the XEOL Analysis of oxygen vacancies in oxide heterostructures. Our main objective was to find a way to directly isolate and see the presence of oxygen vacancies at the interface and extract a depth profile. By using the attenuation length of the materials involved in our samples an then the Beer-Lambert law we calculated a theoretical XEOL and assumed a particular parametrized profile shape, and fit the resulting simulated XEOL energy dependence to experiment by varying the parameters of the profile. Based on the features in the XEOL spectra, the results are divided into high wavelength region and low wavelength region analysed using a curve fitting function. The luminescence profile fitting result of Al_2O_3 grown on top of a substrate STO shows a component that gives a profile spreading about 100 nm into the bulk using a rectangular function as the assumed profile in low wavelength region and a luminescence profile that extends very deep into the substrate using a step function as an assumed profile to get the optimum results in the high wavelength region. The presence of two different vacancy distributions can be due to the vacancies coming from the growth process and perhaps the distribution in the high wavelength region is due to a type of impurities that are evenly spread out through the STO substrate even before the growth procedure. Results of the $LaAlO_3$/STO sample in the low wavelength region shows a luminescence profile that is localized at the very surface of the film which might be due to defects or vacancies at the LAO surface. Using a Gaussian profile the results in high wavelength region show a luminescence profile in which the vacancies are localized near the interface. The results are in agreement with the expected behavior of the vacancies which contribute electrons to form the 2DEG. By consulting the earlier reports and our promising results being consistent with our expectations, there is a strong argument that these defects which are providing the luminescence can in fact be caused by the oxygen vacancies. Comparing the results from these two different samples results in useful gatherings such as the importance of growth condition and how if the sample is grown in high temperatures the vacancies will be homogeneously spread through the bulk, how changes in the optical luminescence spectra can indicate the position and localization of the vacancies abruptly.

5.1 Future Works

5.1.1 $LaTiO_3/LaFeO_3$ Heterostructures Project

The detailed RXR analysis results of one of the samples was presented for this project. Based on the good agreement of the method and fitting process, the analysis of the other two more complicated samples could be a promising project to be tackled in the future. Also the Ti valence change observed near the interface in the $SrTiO_3$ which is a result of the polar discontinuity at the interface can be studied in more detail. Overall the results shown for this project is a strong first step which may provide insight into useful functionalities of the interface and possible use in electronic and magnetic devices. Further theoretical studies could investigate why the Fe^{2+} spin state is high spin while earlier theoretical work predicted low spin. Perhaps the two spin states are very close in energy for this system, and could be harnessed for magnetic switching applications.

5.1.2 XEOL Analysis of Oxygen Vacancies in Heterostructures project

In XEOL measurements another control parameter can be the incident angle of the photons on the film surfaces and thus varying the probing depth. The results presented for two of our samples indicates that XEOL proves to be ideal for the process of extraction of a depth profile of oxygen vacancies in oxide heterostructures. The next step would be to apply the method to other samples with Yttria-Stabilized Zirconia (YSZ) capping or samples with different thicknesses of buffer layers. Our results could be a reference for further understanding of the oxygen vacancy system which can be a huge leap forward to mobility enhancement and device applications.

References

[1] Rolf E Hummel. *Understanding materials science: history, properties, applications*. Springer Science & Business Media, 2004.

[2] Douglas C Hofmann and SN Roberts. Microgravity metal processing: from undercooled liquids to bulk metallic glasses. *npj Microgravity*, 1(1):1–10, 2015.

[3] J Kleibeuker, Z Zhong, H Nishikawa, J Gabel, A Müller, F Pfaff, M Sing, K Held, R Claessen, G Koster, and G. Rijnders. Electronic reconstruction at the isopolar latio 3 / - 3 interface: An x-ray photoemission and density-functional theory study. *Physical Review Letters*, 113:237402, 12 2014.

[4] JE Hamann-Borrero, S Macke, WS Choi, R Sutarto, F He, A Radi, I Elfimov, RJ Green, MW Haverkort, VB Zabolotnyy, et al. Valence-state reflectometry of complex oxide heterointerfaces. *npj Quantum Materials*, 1:16013, 2016.

[5] Sebastian Macke, A Radi, J Hamann Borrero, M Bluschke, S Brück, E Goering, R Sutarto, F He, G Cristiani, M Wu, E Benckiser, H.-U Habermeier, G Logvenov, N Gauquelin, G Botton, A Kajdos, S Stemmer, G Sawatzky, M Haverkort, and V. Hinkov. Element specific monolayer depth profiling. *Advanced Materials*, 26, 10 2014.

[6] JE Kleibeuker, Z Zhong, H Nishikawa, J Gabel, A Müller, F Pfaff, M Sing, K Held, R Claessen, G Koster, et al. Electronic reconstruction at the isopolar latio 3/lafeo 3 interface: an x-ray photoemission and density-functional theory study. *Physical Review Letters*, 113(23):237402, 2014.

[7] Daniel Khomskii. *Transition metal compounds*. Cambridge University Press, 2014.

[8] Robert Green. *Transition metal impurities in semiconductors: induced magnetism and band gap engineering*. PhD thesis, Citeseer, 2013.

[9] MCAT Content. Transition metals. `https://jackwestin.com/resources/mcat-content/the-periodic-table-classification-of-elements-into-groups-by-electronic-structure/transition-metals`, 2020. [Online; accessed 28-January-2021].

[10] Harold H Kung. *Transition metal oxides: surface chemistry and catalysis*. Elsevier, 1989.

[11] Wikipedia contributors. Lanthanum aluminate-strontium titanate interface — Wikipedia, the free encyclopedia. `https://en.wikipedia.org/w/index.php?title=Lanthanum_aluminate-strontium_titanate_interface&oldid=890378339`, 2019. [Online; accessed 11-August-2019].

[12] Wikipedia contributors. Superconductivity — Wikipedia, the free encyclopedia. `https://en.wikipedia.org/w/index.php?title=Superconductivity&oldid=910988466`, 2019. [Online; accessed 21-August-2019].

[13] Wikipedia contributors. Surface properties of transition metal oxides — Wikipedia, the free encyclopedia. https://en.wikipedia.org/w/index.php?title=Surface_properties_of_transition_metal_oxides&oldid=884527219, 2019. [Online; accessed 21-August-2019].

[14] Wikipedia contributors. Perovskite (structure) — Wikipedia, the free encyclopedia. https://en.wikipedia.org/w/index.php?title=Perovskite_(structure)&oldid=907221702, 2019. [Online; accessed 21-August-2019].

[15] Wikipedia contributors. Titanium — Wikipedia, the free encyclopedia. https://en.wikipedia.org/w/index.php?title=Titanium&oldid=910235047, 2019. [Online; accessed 21-August-2019].

[16] Wikipedia contributors. Heterojunction — Wikipedia, the free encyclopedia, 2020. [Online; accessed 4-May-2020].

[17] Yunzhong Chen and RJ Green. Progress and perspectives of atomically engineered perovskite oxide interfaces for electronics and electrocatalysts. *Advanced Materials Interfaces*, 6(15):1900547, 2019.

[18] Milton Ohring. *Materials science of thin films*. Elsevier, 2001.

[19] AD Caviglia, S Gariglio, N Reyren, D Jaccard, T Schneider, M Gabay, Stefan Thiel, G Hammerl, J Mannhart, and J-M Triscone. Electric field control of the laalo 3/srtio 3 interface ground state. *Nature*, 456(7222):624–627, 2008.

[20] Nicolas Reyren, S Thiel, AD Caviglia, LF Kourkoutis, G Hammerl, C Richter, CW Schneider, T Kopp, A-S Rüetschi, D Jaccard, et al. Superconducting interfaces between insulating oxides. *Science*, 317(5842):1196–1199, 2007.

[21] Greg Parker. *Encyclopedia of materials: science and technology*. Elsevier, 2001.

[22] S Macke, A Radi, JE Hamann-Borrero, A Verna, M Bluschke, S Brück, E Goering, R Sutarto, F He, G Cristiani, et al. Element specific monolayer depth profiling. *Advanced Materials*, 26(38):6554–6559, 2014.

[23] Albert C Thompson, D Vaughan, et al. *X-ray data booklet*, volume 8. Lawrence Berkeley National Laboratory, University of California Berkeley, CA, 2001.

[24] Arthur Stanton. Wilhelm conrad röntgen on a new kind of rays: translation of a paper read before the würzburg physical and medical society, 1895. *Nature*, 53(1369):274–276, 1896.

[25] Philip Willmott. *An introduction to synchrotron radiation: techniques and applications*. John Wiley & Sons, 2019.

[26] Light sources of the world – lightsources.org. https://lightsources.org/lightsources-of-the-world/. (Accessed on 06/15/2020).

[27] Education — canadian light source. https://www.lightsource.ca/education.html. (Accessed on 06/15/2020).

[28] Wikipedia contributors. X-ray photoelectron spectroscopy — Wikipedia, the free encyclopedia. https://en.wikipedia.org/w/index.php?title=X-ray_photoelectron_spectroscopy&oldid=961872033, 2020. [Online; accessed 15-June-2020].

[29] Jeroen A Van Bokhoven and C Lamberti. *X-ray absorption and X-ray emission spectroscopy: theory and applications*, volume 1. John Wiley & Sons, 2016.

[30] FMF De Groot and A Kotani. *Core Level Spectroscopy of Solids*. Taylor & Francis CRC Press, 2008.

[31] Frank De Groot and Akio Kotani. *Core level spectroscopy of solids*. CRC press, 2008.

[32] Wikipedia contributors. X-ray absorption near edge structure — Wikipedia, the free encyclopedia. `https://en.wikipedia.org/w/index.php?title=X-ray_absorption_near_edge_structure&oldid=960185122`, 2020. [Online; accessed 15-June-2020].

[33] Matthew Newville. Fundamentals of xafs. *Reviews in Mineralogy and Geochemistry*, 78(1):33–74, 2014.

[34] RJ Green, R Sutarto, F He, M Hepting, DG Hawthorn, and GA Sawatzky. Resonant soft x-ray reflectometry and diffraction studies of emergent phenomena in oxide heterostructures. *Synchrotron Radiation News*, 33(2):20–24, 2020.

[35] Grant S Henderson, FMF De Groot, and BJA Moulton. X-ray absorption near-edge structure (xanes) spectroscopy. *Reviews in Mineralogy and Geochemistry*, 78(1):75–138, 2014.

[36] Claude André Degueldre. *The analysis of nuclear materials and their environments*. Springer, 2017.

[37] M Zwiebler, JE Hamann-Borrero, M Vafaee, P Komissinskiy, S Macke, R Sutarto, F He, B Büchner, GA Sawatzky, L Alff, et al. Electronic depth profiles with atomic layer resolution from resonant soft x-ray reflectivity. *New Journal of Physics*, 17(8):083046, 2015.

[38] S Macke and E Goering. Magnetic reflectometry of heterostructures. *Journal of Physics: Condensed Matter*, 26(36):363201, 2014.

[39] Wikipedia contributors. X-ray reflectivity — Wikipedia, the free encyclopedia. `https://en.wikipedia.org/w/index.php?title=X-ray_reflectivity&oldid=960416324`, 2020. [Online; accessed 16-June-2020].

[40] Charles Kittel and P McEuen. *Introduction to solid state physics*, volume 8. Wiley New York, 1996.

[41] V Holy, J Kubena, I Ohli, K Lischka, W Plotz, et al. X-ray reflection from rough layered systems. *Physical Review B*, 47(23):15896, 1993.

[42] Luuk JP Ament, M Van Veenendaal, TP Devereaux, JP Hill, and J Van Den Brink. Resonant inelastic x-ray scattering studies of elementary excitations. *Reviews of Modern Physics*, 83(2):705, 2011.

[43] X-ray excited optical luminescence (xeol) - online dictionary of crystallography. `https://dictionary.iucr.org/X-ray_excited_optical_luminescence_(XEOL)`. (Accessed on 06/15/2020).

[44] TK Sham, R Sammynaiken, YJ Zhu, P Zhang, I Coulthard, and SJ Naftel. X-ray excited optical luminescence (xeol): a potential tool for oeld studies. *Thin Solid Films*, 363(1-2):318–321, 2000.

[45] Lijia Liu. *X-ray Absorption Fine Structure and X-ray Excited Optical Luminescence Studies of One-dimensional Nanomaterials*. PhD thesis, The University of Western Ontario, 2012.

[46] L Soderholm, GK Liu, Mark R Antonio, and FW Lytle. X-ray excited optical luminescence (xeol) detection of x-ray absorption fine structure (xafs). *The Journal of Chemical Physics*, 109(16):6745–6752, 1998.

[47] Zhang Zhao-Hong, Z Jiang, X Song, and Z Li-Fang. Time structure measurement of the ssrf storage ring using trxeol method. *Nuclear Science and Techniques*, 26, 08 2015.

[48] Wikipedia contributors. Photoluminescence — Wikipedia, the free encyclopedia. `https://en.wikipedia.org/w/index.php?title=Photoluminescence&oldid=944982183`, 2020. [Online; accessed 16-June-2020].

[49] Wikipedia contributors. Spin states (d electrons) — Wikipedia, the free encyclopedia. `https://en.wikipedia.org/w/index.php?title=Spin_states_(d_electrons)&oldid=886962353`, 2019. [Online; accessed 21-August-2019].

[50] S Macke, JE Hamann-Borrero, RJ Green, B Keimer, GA Sawatzky, and MW Haverkort. Dynamical effects in resonant x-ray diffraction. *Physical Review Letters*, 117(11):115501, 2016.

[51] Maurits W. Haverkort et al. Quanty - a quantum many body script language — quanty, 2019. [Online; accessed 22-August-2019].

[52] M Zwiebler, E Di Gennaro, JE Hamann-Borrero, T Ritschel, RJ Green, GA Sawatzky, E Schierle, E Weschke, A Leo, F Miletto Granozio, et al. Transition from a uni-to a bimodal interfacial charge distribution in laalo3/srtio3 upon cooling. *Scientific Reports*, 10(1), 2020.

[53] Robert J Green, T Z Regier, B Leedahl, J A McLeod, X H Xu, G S Chang, E Z Kurmaev, and A Moewes. Adjacent fe-vacancy interactions as the origin of room temperature ferromagnetism in $(\mathrm{in}_{1-x}\mathrm{fe}_x)_2\mathrm{o}_3$. *Physical Review Letters*, 115:167401, Oct 2015.

[54] T Haupricht, R Sutarto, M W. Haverkort, H Ott, A Tanaka, H H Hsieh, H.-J Lin, C T Chen, Z Hu, and L H Tjeng. Local electronic structure of fe2+ impurities in mgo thin films: Temperature-dependent soft x-ray absorption spectroscopy study. *Physical Review B*, 82:035120, Jul 2010.

[55] A Ohtomo and HY Hwang. A high-mobility electron gas at the laalo 3/srtio 3 heterointerface. *Nature*, 427(6973):423–426, 2004.

[56] Alexander Brinkman, M Huijben, M Van Zalk, J Huijben, U Zeitler, JC Maan, WG van der Wiel, GJHM Rijnders, D HA Blank, and H Hilgenkamp. Magnetic effects at the interface between non-magnetic oxides. *Nature Materials*, 6(7):493–496, 2007.

[57] Harold Y Hwang, Y Iwasa, M Kawasaki, B Keimer, N Nagaosa, and Y Tokura. Emergent phenomena at oxide interfaces. *Nature Materials*, 11(2):103–113, 2012.

[58] Yunzhong Chen, N Pryds, JE Kleibeuker, G Koster, J Sun, E Stamate, B Shen, G Rijnders, and S Linderoth. Metallic and insulating interfaces of amorphous srtio3-based oxide heterostructures. *Nano Letters*, 11(9):3774–3778, 2011.

[59] YZ Chen, Felix Trier, Tom Wijnands, RJ Green, N Gauquelin, R Egoavil, Dennis Valbjørn Christensen, G Koster, M Huijben, N Bovet, et al. Extreme mobility enhancement of two-dimensional electron gases at oxide interfaces by charge-transfer-induced modulation doping. *Nature Materials*, 14(8):801–806, 2015.

[60] Yanwu Xie, C Bell, Y Hikita, S Harashima, and HY Hwang. Enhancing electron mobility at the laalo3/srtio3 interface by surface control. *Advanced Materials*, 25(34):4735–4738, 2013.

[61] Mark Huijben, G Koster, MK Kruize, S Wenderich, J Verbeeck, S Bals, E Slooten, B Shi, HJA Molegraaf, JE Kleibeuker, et al. Defect engineering in oxide heterostructures by enhanced oxygen surface exchange. *Advanced Functional Materials*, 23(42):5240–5248, 2013.

[62] ZQ Liu, CJ Li, WM Lü, XH Huang, Z Huang, SW Zeng, XP Qiu, LS Huang, A Annadi, JS Chen, et al. Origin of the two-dimensional electron gas at laalo 3/srtio 3 interfaces: the role of oxygen vacancies and electronic reconstruction. *Physical Review X*, 3(2):021010, 2013.

[63] YF Hu, L Zuin, G Wright, R Igarashi, M McKibben, T Wilson, SY Chen, T Johnson, D Maxwell, BW Yates, et al. Commissioning and performance of the variable line spacing plane grating monochromator beamline at the canadian light source. *Review of Scientific Instruments*, 78(8):083109, 2007.

[64] R Reininger, K Tan, and I Coulthard. An insertion device beamline for 5–250 ev at the canadian light source. *Review of Scientific Instruments*, 73(3):1489–1491, 2002.